International Journal of Thermophysics (2026) 47:168
https://doi.org/10.1007/s10765-026-03808-5

Viscosity and Interfacial Tension of γ-Butyrolactone, 1,4-Butanediol, and Their Mixtures by Surface Light Scattering and Conventional Methods

Yongzhen Sun[1] · Julius Hans Jander[1] · Yang Xie[1] · Muhammad Junaid Akhtar[1] · Michael Heinrich Rausch[1] · Michael Geißelbrecht[2] · Peter Wasserscheid[2,3,4] · Andreas Paul Fröba[1]

Received: 10 June 2026 / Accepted: 30 June 2026 / Published online: 7 October 2026
© The Author(s) 2026

Abstract

Liquid organic hydrogen carrier (LOHC) systems are regarded as a promising option for the safe and efficient storage and transport of hydrogen (H_2). For the LOHC system based on γ-butyrolactone (GBL) and 1,4-butanediol (BDO) that is discussed as a biogenic and biodegradable alternative to fossil-based aromatic/alicyclic LOHC systems, reliable thermophysical property data like liquid dynamic viscosity η_L and interfacial tension σ are still scarce, particularly under process-relevant conditions. This work summarizes the results from recent research activities on the determination of η_L and σ for GBL, BDO, and their binary mixtures with GBL amount fractions of $x_{GBL} = (0.25,\ 0.50,\ \text{and}\ 0.75)$ at temperatures T up to 473 K at a pressure of about 0.1 MPa. Surface light scattering (SLS) was applied for the simultaneous measurement of η_L and σ, complemented by capillary viscometry and pendant drop measurements, while polarization-difference Raman spectroscopy was employed during the SLS experiments to monitor the mixture composition. Observed changes of the latter at elevated T partially restricted a reliable property determination. Within the stable T range, σ decreases continuously with increasing T and increasing x_{GBL}. η_L decreases strongly with increasing x_{GBL}, presumably because of the breaking of the strong hydrogen bonds between BDO molecules.

Keywords Liquid organic hydrogen carriers · Viscosity · Interfacial tension · Surface light scattering · Pendant drop method · Capillary viscometry · Raman spectroscopy

Extended author information available on the last page of the article

1 Introduction

For the global transition toward an energy system mainly relying on renewable resources, the efficient and safe storage and transport of hydrogen (H_2) remain critical challenges. Conventional approaches such as compression to pressures up to 70 MPa [1] or cryogenic liquefaction below 20 K [2, 3] require significant energy input and costly equipment and infrastructure, motivating the development of alternative storage technologies. Among the various candidates, liquid organic hydrogen carrier (LOHC) systems have attracted increasing attention due to their favorable volumetric and gravimetric H_2 storage densities, their compatibility with existing fuel infrastructure, and the possibility of reversible hydrogenation/dehydrogenation cycles under technically feasible conditions [4–7].

In the past few years, significant progress has been made in LOHC-related research and technology development, particularly in connection with LOHC systems based on the dehydrogenated compounds toluene [8], diphenylmethane [9–11], benzyltoluene [12], dibenzyltoluene [4, 13, 14], and related compounds and mixtures. Although these aromatic/alicyclic-based LOHC systems offer advantages such as high thermal stability and convenient physical properties, several challenges persist. Respective examples are high dehydrogenation temperatures [15, 16], catalyst deactivation [17, 18], and by-product formation during cycling [19], which may compromise their long-term applicability. Furthermore, careful consideration of the environmental impact of these aromatic hydrocarbons, especially regarding aquatic toxicity, is necessary [20].

In the view of these limitations and the increasing demand for sustainable chemical processes, LOHC systems containing heteroatoms such as nitrogen or oxygen have attracted growing attention. Such systems like those based on dibenzofuran [21] and 6-methoxy-quinoline [22] generally require milder conditions for H_2 uptake and release compared to purely hydrocarbon-based LOHC systems. The LOHC system based on the hydrogen-lean compound γ-butyrolactone (GBL) and the fully hydrogenated compound 1,4-butanediol (BDO) is of particular interest in this work because it provides in addition a favorable environmental profile including accessibility from biomass and good biodegradability of all compounds involved [23–25]. Although the gravimetric H_2 storage capacity of the GBL/BDO system is relatively modest at 4.4 wt%, the system offers an attractive volumetric H_2 storage density of 45 kg(H_2)·m^{-3} thanks to the comparatively large liquid density of BDO [26].

Recent studies demonstrate that the hydrogenation of GBL to BDO is feasible in a temperature range from $T \approx$ (373 to 473) K and H_2 pressures up to about 4 MPa [27–29]. For the efficient design and optimization of LOHC processes, accurate knowledge of thermophysical properties such as liquid dynamic viscosity η_L and interfacial tension σ under corresponding conditions is indispensable, as these parameters govern processes related to fluid dynamics, heat and mass transfer, and catalyst wetting in hydrogenation and dehydrogenation reactors. While extensive η_L and σ data have been reported for aromatic/alicyclic hydrocarbon-based LOHC systems in the past few years, comparable investigations for the GBL/BDO system

are largely missing. To the best of the authors' knowledge, reliable experimental data for σ of GBL are limited in the open literature. A single data point at $T = 293$ K is reported in the online database PubChem [30], which refers to Ref. [31]. Further data have been reported using the capillary rise method up to $T = 343$ K [32] and the platinum plate method up to $T = 323$ K [33]. For η_L of GBL, available data cover only narrow T ranges up to approximately 333 K and originate from rolling-ball viscometry [34], rotational viscometry [35], and capillary viscometry [36–38]. Although more data for σ are available for BDO, most published studies provide only a single data point [39–41]. In contrast, Liu et al. [42] and Kong et al. [43] measured σ in the T range from (293.15 to 318.15) K using a calibrated surface tensiometer. η_L was also measured in both studies using capillary viscometry. For η_L of BDO, additional datasets extending up to $T = 422.9$ K have been published [44]. Most of the available studies rely on capillary viscometry as well [42–47], whereas Lech et al. [48] reported results obtained with a rotational viscometer.

This summary shows that the availability of η_L and σ data for the pure compounds of the GBL/BDO LOHC system is rather limited and does not fully cover the process-relevant T range even in the absence of H_2. Moreover, data for corresponding binary mixtures occurring during the LOHC-related processes are lacking completely. Picking this situation up, this work summarizes the results from recent research activities on the determination of η_L and σ for GBL, BDO, and their binary mixtures with GBL amount fractions of $x_{GBL} = (0.25, 0.50,$ and $0.75)$ in the T range from (298 to 473) K at about 0.1 MPa. Surface light scattering (SLS) was applied for the simultaneous measurement of η_L and σ, while additional data were obtained by capillary viscometry (CV) and the pendant drop method (PD) to complement the SLS data and for mutual comparison. Addressing the experience from a previous study focusing on the thermal conductivity, density, thermal diffusivity, and mass diffusivity of the same LOHC system [49], special care was taken with respect to sample stability during measurement series. In this connection, polarization-difference Raman spectroscopy (PDRS) was applied to the liquid bulk of the sample during SLS experiments. After an introduction of the experimental methods and procedures, observations and conclusions regarding sample stability are discussed first since they need to be considered in the subsequent presentation of the measured data sets.

2 Experimental Section

2.1 Materials and Sample Preparation

The relevant information about the characteristics of the materials employed in this work, including their CAS numbers, suppliers, molar masses M, critical temperatures T_c, and purities, is summarized in Table 1. All liquids and components used in this study were handled under dry argon (Ar) atmosphere to minimize exposure to moisture and other contaminants. Before use, all glass vessels, stainless-steel parts, and tubing that contact the samples were cleaned sequentially with soap solution, cleaning benzine, ethanol, acetone, and deionized water, and were finally dried with

Table 1 Specification of the supplier, molar mass M, critical temperature T_c, and purities in terms of mass fraction w or volume fraction Φ of the chemicals used

Substance	CAS number	Supplier	Molar mass M / (g·mol^{-1})	Critical temperature T_c / K	Specified purity[a]
γ-Butyrolactone (GBL)	96-48-0	Thermo Fisher Scientific	86.09	731[b]	$w = 0.999$
1,4-Butanediol (BDO)	110-63-4	Thermo Fisher Scientific	90.12	727[b]	Batch 1: $w = 0.995$ Batch 2: $w = 0.996$
Hydrogen (H_2)	1333-74-0	Air Liquide Deutschland GmbH	2.02	33.15[a]	$\Phi \geq 0.999999$
Argon (Ar)	7440-37-1	Air Liquide Deutschland GmbH	39.95	150.85[c]	$\Phi \geq 0.99999$

[a] As specified by the manufacturer in the certificate of analysis for the used batch

[b] Reference [88]

[c] Reference [89]

filtered compressed air. This ensures that all surfaces in the system are free from any residual impurities and moisture.

The preparation of all binary mixtures of GBL and BDO with amount fractions of GBL of $x_{GBL} = (0.25, 0.50, \text{and } 0.75)$ was carried out gravimetrically using a balance with a precision of 0.1 mg and an expanded uncertainty (coverage factor $k = 2$) of $U(m) = 1$ mg for the mass m. On this basis, the absolute expanded uncertainty ($k = 2$) of x_{GBL} can be specified with $U(x_{GBL}) = 0.000003$ for the mixtures used for measurements with SLS, CV, and PD. The exact compositions of the samples used for different fillings of the dedicated setups are listed in Table 2. For their calculation, impurities in the pure GBL and BDO used for mixture preparation were not considered. For the mixtures, further fillings of the SLS cell were studied with respect to stability aspects. These are not included in Table 2 because no reliable thermophysical property data could be obtained from respective experiments.

Prior to each measurement, the samples were filtered at least twice to remove particulate impurities. A two-stage filtration unit combining hydrophilic polytetrafluoroethylene (H-PTFE) membrane filters with pore sizes of (0.45 and 0.20) µm was used. The water contents in terms of the water mass fraction w_{H2O} were determined by Karl Fischer coulometric titration with a relative expanded uncertainty ($k = 2$) of less than 20%. This was done after the filtration as well as after finishing measurement series by CV covering T up to 348 K and by SLS, where the corresponding results are given in Table 2. For all samples, the w_{H2O} values before the experiments were below about 500 ppm and increased to a maximum of about 4000 ppm after the experiments, which will be discussed in Sect. 3.1. For the samples studied by CV at $T > 348$ K and by PD, w_{H2O} was not measured after the experiments due to unavoidable contamination during capillary removal from the high-T CV setup and a too small sample amount available after the PD measurements.

Table 2 Sample composition and results from water content measurements of the investigated samples before and after measurements by SLS, CV, and PD[a,b]

System	Measurement or filling[a]	x_{GBL}[b]	T range / K[c]	w_{H2O} / ppm	
				Before	After
GBL	SLS-1	1.000000	323	50	1600
	SLS-2		348	200	2300
	SLS-3		298–373	200	2000
	CV-1		298–348	80	460
	CV-2		298–348	120	310
	CV-3		348–473	200	–
	CV-4		298–473	200	–
	PD-1		298–423	200	–
	PD-2		298–473	200	–
	PD-3		423–473	200	–
BDO	SLS-1	0.000000	298–473	500	1800
	SLS-2		348–473	300	2200
	CV-1		298–348	440	860
	CV-2		348–473	300	–
	CV-3		373–473	300	–
	PD-1		295–373	300	–
	PD-2		303–448	300	–
	PD-3		423–473	300	
$x_{GBL} = 0.25$	SLS-1	0.251247	298–398	370	2000
	SLS-2	0.251350	348	350	2600
	CV-1	0.251247	298–348	370	730
	CV-2	0.251350	348–373	350	–
	CV-3	0.251350	373	350	–
	PD-1	0.251350	293–473	350	–
$x_{GBL} = 0.50$	SLS-1	0.499620	298–373	310	1100
	SLS-2	0.500188	323	200	3000
	CV-1	0.499620	298–323	80	230
	CV-2	0.500188	323–348	200	420
	PD-1	0.500188	293–473	200	–
$x_{GBL} = 0.75$	SLS-1	0.748977	298–473	500	700
	SLS-2	0.749078	303–423	300	1000
	SLS-3	0.749078	348	300	2000
	CV-1	0.748977	303–348	410	820
	CV-2	0.749220	298–323	290	500
	CV-3	0.749220	298–303	290	460
	CV-4	0.749220	348–373	290	–
	PD-1	0.749220	295–373	290	–
	PD-2	0.749220	303–448	290	–

[a]For the measurements with the first and second filling of the SLS cell with pure BDO, batches 1 and 2 were used, respectively. All mixtures were prepared with batch 1 of BDO

[b]The reported x_{GBL} values do not consider any impurities in the pure substances. The uncertainty of x_{GBL} for the mixtures is $U(x_{GBL})=0.000003$, while the relative uncertainty of the water content is $U_r(w_{H2O})<0.2$

[c]The reported T range covers the full range to which the individual samples had been exposed, while not all corresponding measurements contributed to the final experimental data reported in this work

2.2 Surface Light Scattering: Dynamic Viscosity and Interfacial Tension

SLS provides the possibility to accurately determine η_L and σ of fluids in macroscopic thermodynamic equilibrium in a contactless manner without any calibration procedure. It relies on the facts that the dynamics of surface fluctuations naturally occurring at fluid phase boundaries due to molecular motion are governed by these properties and that corresponding information can be found in light that is scattered elastically in this region. In the last decades, SLS was applied for the investigation of various types of working fluids relevant for chemical and energy engineering, such as refrigerants [50], hydrocarbons [51, 52], ionic liquids[53, 54], and various LOHC systems [9, 55, 56]. While more details on the method are available in specialized literature [57–59], the main aspects relevant for the present study are summarized in the following.

The light source is a frequency-doubled Nd:YVO_4 laser with a wavelength of $\lambda_0 = 532$ nm, where the laser power incident to the surface is kept below 30 mW to avoid local heating. At a given state point, the light scattered perpendicular to the fluid interface is analyzed at different moduli of the wave vector, $q = (2\pi \ / \ \lambda_0) \ \sin(\Theta_I)$ [57, 59], adjusted by varying external incident angles Θ_I of (3.0, 3.1, and 3.2)°. To minimize alignment errors, the same Θ_I are adjusted on both sides of the surface normal so that six independent measurements are performed. After leaving the measurement cell, the scattered light is superimposed with coherent reference light of higher intensity to achieve heterodyne conditions and is then detected by single-photon detectors like, in the present case, an avalanche photodiode system. The corresponding signals are processed by a linear-tau correlator to obtain the normalized intensity correlation function (CF) [51]. In general, the temporal evolution of surface fluctuations represented in the CFs as a function of the delay time τ can be classified into two cases that are distinguished via the reduced capillary number Y. The latter is defined as $Y = \rho_L \cdot \sigma \cdot (4{\eta_L}^2 \cdot q)^{-1}$. For fluids with comparatively low η_L and/or high σ yielding $Y > 0.145$, the fluctuations exhibit a damped oscillatory behavior. In this case, the corresponding CF can be represented by

$$g^{(2)}(\tau) = a + b \cdot \cos(\omega_q \cdot |\tau| - \phi) \cdot \exp(-|\tau|/\tau_C) + c \cdot \exp(-|\tau|/\tau_{C,bulk}). \quad (1)$$

This theoretical model includes the experimental constants a, b, and c as well as the phase factor ϕ that mainly accounts for minor deviations from the ideal Lorentzian line shape of the related power spectrum [60]. The mean lifetime τ_C, corresponding to the damping rate $\Gamma = {\tau_C}^{-1}$, and the oscillation frequency ω_q characterize the dynamic behavior of the surface waves. The additional exponential term with the decay time $\tau_{C,bulk}$ is only relevant for Y values between about 0.4 and 15. It accounts for minor contributions from the rotational flow in the bulk of the fluid, which is associated with a coupling between the motion of the surface and that of the bulk phase, leading to a delayed response of the surface fluctuation dynamics probed by SLS. Such conditions apply only in specific T ranges for the different systems studied

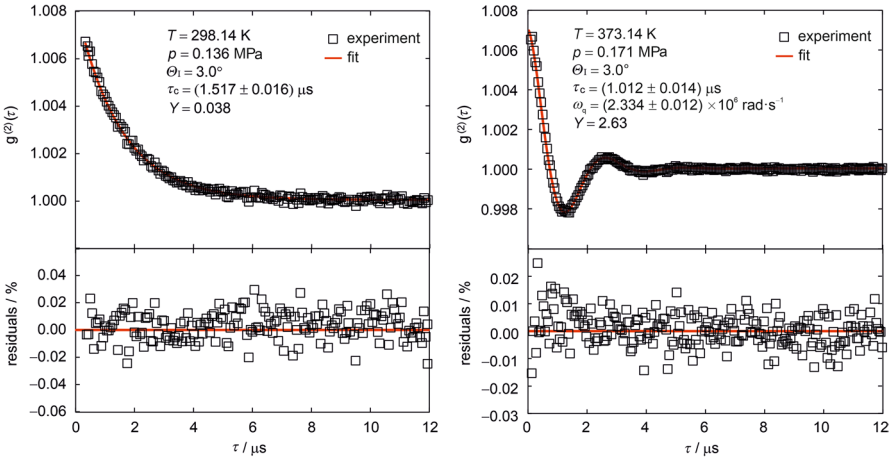


Fig. 1 Examples of experimental CFs including their residuals with respect to the fits according to Eqs. 1 and 2 obtained by SLS for the mixture with $x_{GBL}=0.25$ close to $p=0.1$ MPa at $T=298.14$ K (left) and $T=373.14$ K (right) as a function of the delay time τ. In the right example, the contribution related to the rotational flow in the bulk of the fluid was considered in the fitting procedure

here, which are (298 and 323) K for GBL, (398 to 448) K for BDO, 373 K for the mixture with $x_{GBL}=0.25$, (323 and 348) K for the mixture with $x_{GBL}=0.50$, and (298 to 373) K for the mixture with $x_{GBL}=0.75$. More details on the corresponding background and on how $\tau_{C,bulk}$ is determined are given in Ref. [60].

For fluids with relatively high η_L and/or low σ, resulting in $Y\leq 0.145$, the fluctuations are overdamped and non-propagating ($\omega_q=0$). Then, the corresponding CF can be represented by

$$g^{(2)}(\tau) = a + b \cdot \exp\left(-|\tau|/\tau_C\right). \tag{2}$$

Here, τ_C only gives information with respect to the ratio of η_L to σ, where σ data from PD are used as further input for the evaluation of the SLS experiments aiming at the determination of η_L [57, 61]. This situation applies, e.g., to BDO at T up to 348 K and to the mixture with $x_{GBL}=0.25$ at (348 and 373) K. Figure 1 shows examples for CFs that were recorded for the mixture with $x_{GBL}=0.25$ at T of 298.14 K (left) and 373.14 K (right) and represent an overdamped and a damped oscillatory case, respectively. The absence of systematic deviations in the residual plots in the lower part of Fig. 1 confirms that the experimental data are consistent with the theoretical descriptions according to Eqs. 1 and 2. The obtained τ_C and ω_q values are used in the final evaluation step with respect to η_L and σ, where the corresponding fit uncertainties displayed in Fig. 1 are given on a confidence level of 95% ($k=2$). The average relative uncertainties for τ_C and ω_q considering all evaluated CFs are $U_r(\tau_C)=2.8\%$ and $U_r(\omega_q)=1.3\%$.

To accurately solve the dispersion relation $D(\eta_L, \eta_G, \rho_L, \rho_G, \sigma, \tau_C, \omega_q, q)$ in its entire form for the interface between a liquid (index L) and a gas (index G) phase,

the directly measured data for τ_C and ω_q together with the given q are combined with reference data for the density of the liquid phase, ρ_L, and of the gas phase, ρ_G, as well as with the dynamic viscosity of the gas phase, η_G. Further details on the reference data employed are given in section S1 in the Supporting Information. In this work, SLS experiments were performed with a cylindrical stainless-steel sample cell designed for operation with H_2, where the cell axis is oriented horizontally. The measurements were performed at about 0.1 MPa of H_2 atmosphere at nine T of (298, 303, 323, 348, 373, 398, 423, 448, and 473) K. The cell was leak-tested with He before each measurement series to ensure tightness. After the liquid had been filled into the sample cell with a glass syringe, the system was flushed several times with H_2 to about 0.4 MPa and then adjusted to a final p roughly 0.1 MPa above the vapor pressure of the sample. The T control of the sample cell was achieved by resistance heating. T was measured by three Pt100 resistance probes calibrated with an expanded ($k=2$) uncertainty of $U(T)=0.02$ K that are inserted into the main cell body. One probe located near the outer cell wall was used for T control. The data obtained with the other two probes positioned close to the opposite ends of the gas–liquid interface were averaged to define the reported measurement T. When needed, the power supplied to a supplementary heating wire attached to one side of the cell is adjusted to reduce any T differences between both sides [62], resulting in a remaining horizontal T deviation over the whole cell that is typically below 0.02 K. p is measured with a high-precision transducer with an expanded uncertainty $U(p)=5$ kPa, while the p drift occurring during the measurements at a given state point is within ± 0.15 kPa. For each state point, T reported in the data tables corresponds to mean values obtained by averaging the individual measurements over the entire recording period. The expanded uncertainties ($k=2$) associated with the reported temperatures, $U(T)$, and pressures, $U(p)$, were determined from the individual T and p measurements. Three contributions were considered. The first arises from the calibration uncertainty of the respective sensors. The second contribution accounts for the short-term stability during the individual recording intervals of the CFs at the different scattering vectors q and was quantified by the average of the doubled standard deviations of the corresponding T and p values recorded while the individual q were studied. The third contribution reflects the overall stability at a given state point and is represented by the doubled standard deviation of the mean T and p values obtained at the different q investigated for that state point. The mean values of η_L and σ obtained from the different CFs for a given filling of the SLS cell and a given T are averaged with a weighting scheme considering their individual uncertainties. In a conservative manner, the largest individual uncertainties among the data from different fillings are reported as final uncertainty for both η_L and σ. Since the corresponding T for different fillings at a given state point in this work are very similar and agree within their combined uncertainties, they were directly averaged to obtain the reported values.

2.3 Polarization-Difference Raman Spectroscopy: Composition

The principle of Raman spectroscopy (RS) is based on the inelastic scattering of monochromatic light. When such light from a laser interacts with molecules, a small fraction of the scattered photons exhibits an energy shift corresponding to molecular vibrational and rotational motions, resulting in a Raman spectrum that can be interpreted as a molecular fingerprint of the scattering material [63, 64]. This can help to identify, e.g., the formation of new compounds during processes. Furthermore, respective calibrations allow to determine the mixture composition via the relation between intensities of Raman bands characteristic for the individual constituents of the mixture. Recently, this approach was successfully applied for the determination of the composition of liquid mixtures related to the LOHC systems based on diphenylmethane [65] and benzyltoluene [66] as well as of binary mixtures of GBL and BDO [49], which gives access to their degree of hydrogenation.

For the latter system being in the focus of the present study, polarization-difference Raman spectroscopy (PDRS) was applied to improve signal quality and to reduce the fluorescence background. Details on the calibration procedure for the determination of the composition of binary GBL/BDO mixtures and the optical setup used for this purpose in a previous study are given in Ref. [49]. The optical arrangement and instrumentation for PDRS integrated in the SLS setup and employed in the present study is described in detail in Ref. [65]. Here, Raman spectra of the scattered light with vertical polarization (V) are recorded under a scattering angle of 90°. This results in polarized or depolarized spectra when incident light with vertical or horizontal (H) polarization is used. From them, the isotropic spectrum I_{iso} is calculated according to

$$I_{\mathrm{iso}}(\nu) = \frac{1}{n^2} \times \sum_{i=1}^{n} \sum_{j=1}^{n} \left[I_{\mathrm{VV}}^{(i)}(\nu) - \gamma I_{\mathrm{HV}}^{(j)}(\nu) \right], \tag{3}$$

where γ is a geometric factor characteristic for the employed optical arrangement [67–69] and equals to 4/3 here. I_{VV} and I_{HV} are the intensities of the polarized and depolarized spectra, respectively, recorded as a function of the Raman shift in terms of the wavenumber ν. The indices i and j represent the numbers of the individual spectra. For each state point, eight I_{VV} and eight I_{HV} spectra were recorded. Each spectrum saved by the spectrometer was averaged over three consecutive integrations of 10 s. The I_{iso} spectra calculated via Eq. (3) were then baseline-corrected using the routine described in Ref. [65] by selecting points in I_{iso} at which no Raman signatures were observed.

Figure 2 shows the relevant ν range of the isotropic spectra obtained at $T = 323$ K for the five systems studied here. For the determination of the composition by PDRS, the peak areas in the regions around $\nu = 1760$ cm^{-1} for C=O bond vibrations in GBL [70], I_{GBL}, and around $\nu = 1085$ cm^{-1} for C–O vibrations in BDO [71], I_{BDO}, and their uncertainties are deduced using a peak-fitting algorithm as described in more detail in Ref. [49]. Since the variations in peak positions are small compared to the band widths, these shifts do not affect the

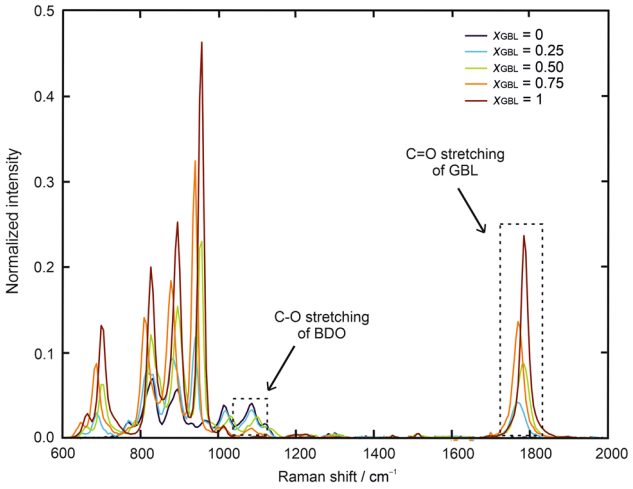


Fig. 2 Isotropic Raman spectra I_{iso} as a function of the Raman shift ν obtained in the liquid phase consisting of GBL and BDO within the SLS setup at $T \approx 323$ K. The dashed rectangles highlight the characteristic vibration modes for GBL around 1760 cm^{-1} and for BDO around 1085 cm^{-1}. Please refer to the online version to distinguish between the different spectra by color

assignment of the characteristic Raman bands or the qualitative interpretation of the spectra significantly. Figure 2 shows that with increasing x_{GBL}, the peak specific for GBL increases while that for BDO decreases.

Based on these peak areas, the intensity ratio I_r can be calculated by

$$I_r = \frac{I_{GBL}}{I_{BDO}}, \tag{4}$$

where the determination of the corresponding expanded ($k=2$) uncertainties $U(I_{GBL})$, $U(I_{BDO})$, and $U(I_r)$ is described in Ref. [49]. This information is used together with the T-independent calibration constant $K=(0.3015 \pm 0.0053)$ ($k=2$) determined in Ref. [49] to obtain x_{GBL} or x_{BDO} via

$$x_{BDO} = 1 - x_{GBL} = \frac{1}{1 + I_r K}. \tag{5}$$

Corresponding uncertainties are obtained based on error propagation calculations in quadrature.

2.4 Pendant Drop Method: Interfacial Tension

The pendant drop method (PD) enables the determination of the interfacial tension σ. It is based on the approach of axisymmetric drop shape analysis (ADSA) [72], in which a theoretical drop profile is fitted to the experimentally obtained drop contour. The theoretical drop profile is described by the Young–Laplace equation

$$\frac{\partial \varphi}{\partial s} = \frac{2}{R_0} - \frac{(\rho_L - \rho_G) g z}{\sigma} - \frac{\sin \varphi}{x}. \tag{6}$$

Here, s denotes the arc length along the projection of the drop contour measured from the apex, while φ represents the angle between the tangent to the drop surface at position s and the horizontal. The coordinates x and z correspond to the horizontal and vertical directions, respectively. R_0 is the radius of curvature at the drop apex, and g denotes the gravitational acceleration. The densities of the liquid drop and surrounding gas phase, ρ_L and ρ_G, are determined as described for the evaluation of SLS experiments in section S1 of the Supplementary Information. A detailed description of the experimental setup [73] and the evaluation procedure [74] can be found in the given references. In the following, relevant details on the procedures applied in the present work are summarized.

The PD experiments were conducted under H_2 atmosphere at approximately 0.1 MPa over nine T of (298, 303, 323, 348, 373, 398, 423, 448, and 473) K. The stainless-steel sample cell used in this setup is equipped with optical windows and resistance heating similar to the SLS setup. The T control and measurement is realized by two Pt-100 resistance probes calibrated with expanded ($k = 2$) uncertainties of $U(T) = 0.02$ K. T measured in the gas phase close to the stainless-steel capillary at which the droplet is formed represents the reported T data. For most measurements, the T stability was within ±0.11 K up to 473 K. Only at the lowest investigated T of each system close to ambient conditions, slightly larger instabilities within a maximum T range of ±0.47 K, but mostly within ±0.25 K were observed. A capillary is mounted at the top of the cell and connected to a glass syringe that contains the liquid sample and is used for forming the droplets. For imaging the PD, a collimated narrow-bandwidth LED light source with a wavelength of 455 nm and a CMOS camera with a resolution of (2456 × 2054) pixels are employed. The outer diameter of the capillary was determined from optical images after using a reference sphere with a diameter of 3.00 mm for pixel-to-length calibration, followed by image analysis using a custom-made MATLAB routine.

Typically, five droplets of a given sample were analyzed at each T, where five images of each droplet were evaluated to ensure statistical reliability. At $T \leq 398$ K, the images of each droplet were recorded after a waiting period of at least 10 min to ensure equilibration, where not significant changes could be observed after longer times. At higher T, the droplets started to wet the outer capillary wall typically about 5 min after droplet formation. This observation will be discussed in more detail in Sect. 3.1. In these cases, five images recorded before this wetting effect occurred were evaluated. For each sample and state point, the reported σ value represents the mean value obtained from all corresponding images of the analyzed droplets. The relative expanded uncertainty ($k = 2$) of the σ data obtained by PD is estimated to be $U_r(\sigma) = 2\%$ for $T \leq 398$ K. This estimate is based on the analysis reported by Jander et al. [73], who compared measurement data obtained with the same experimental setup to reference data for various fluids and state points. The uncertainty accounts for contributions arising from image resolution, T stability, the calibration of

the optical setup, and relative uncertainties of the input ρ_L data of up to 0.3%. For $T > 398$ K, an increased expanded uncertainty of $U_r(\sigma) = 3\%$ is assumed to account for the slight droplet shrinking observed during the measurements. The evaluation of T and p data as well as their uncertainties for the PD measurements was performed analogously to the procedure described for the SLS experiments, where the contributions related to specific drops were determined as explained for specific scattering vectors for SLS. The PD data obtained for the same state point from different fillings of the syringe were averaged arithmetically since the individual uncertainties were comparable and all corresponding data agreed within uncertainties.

2.5 Capillary Viscometry: Viscosity

The liquid kinematic viscosity ν_L was measured using capillary viscometry (CV) with Ubbelohde-type suspended-level glass capillary viscometers. This method relies on the Hagen–Poiseuille principle for laminar flow through a cylindrical tube driven by the hydrostatic pressure of the liquid column above the capillary. ν_L is calculated according to

$$\nu_L = K_{CV} \cdot (t - \Delta t), \tag{7}$$

where K_{CV} is the instrument constant, t is the time it takes for a defined liquid volume to flow through the capillary, and Δt represents the Hagenbach correction accounting for acceleration effects within the flow through the capillary, which was adapted from the corresponding data sheet from the supplier Schott–Geräte GmbH. The liquid dynamic viscosity η_L is obtained from $\eta_L = \rho_L \cdot \nu_L$, where the liquid density ρ_L for the five systems taken from Ref. [49] measured by vibrating-tube densimeters is associated with relative expanded ($k = 2$) uncertainties of $U_r(\rho_L) = 0.02\%$ up to 348 K and 0.1% above this T.

To cover the whole viscosity range for GBL, BDO, and their mixtures from (298 to 473) K, Ubbelohde capillary viscometers of type 0, 0a, 0c, Ic, and IIc were used. The corresponding η_L ranges of the capillaries and their respective K_{CV} values are listed in Table S3 in the Supplementary Information. While the K_{CV} values for the viscometers Ic and IIc originate from the calibration of the supplier, the viscometers 0, 0a, and 0c were calibrated using reference liquids and certified viscosity standards following the procedures described in Refs. [9, 75]. In detail, the viscometer of type 0a was calibrated using *n*-dodecane and the certified viscosity standard S3 (Anton Paar), capillary 0 using *n*-octane and bidistilled water, and capillary 0c using the certified viscosity standard APS3 (Anton Paar).

The viscometers were operated with two complementary setups to cover the full T range. Low-temperature capillary viscometry (LTCV) measurements were conducted with the viscometers immersed in a circulated water bath at (298, 303, 323, and 348) K, where the capillary outlets are in contact with ambient air. For $T \geq 348$ K, a high-temperature capillary viscometer (HTCV) setup equipped with a circulated oil bath was employed and operated under an Ar atmosphere at approximately 0.1 MPa. In both cases, the sample was filled carefully into the viscometers to avoid air bubbles

and equilibrated for several minutes at each target T before measurement. T was measured close to the center of the capillary with a Pt100 resistance probe calibrated with an expanded ($k=2$) uncertainty of $U(T)=0.02$ K. More detailed information on the measurement equipment and procedures for this work can be found in Ref. [10]. The reported T data correspond to mean values obtained from the individual readings over the measurement period. The respective expanded uncertainty ($k=2$) was determined analogously to the procedure described for SLS, where the contributions related to individual runs were obtained as explained for specific scattering vectors for SLS. Consistency between the data obtained with the two systems was verified by measurements at $T=348$ K with the same capillary viscometer in both setups, where the results agreed within uncertainties. For each state point, at least five independent flow times were measured and averaged. They were typically in the range from (150 to 900) s, depending on T and η_L. Following the uncertainty evaluation considering the uncertainties in ρ_L, K_{CV}, and t based on error propagation in quadrature as described in detail in Ref. [58], the overall relative expanded ($k=2$) uncertainty $U_r(\eta_L)$ is below 1.0% for most cases, with only a slightly increased value of 1.5% obtained at $T=373$ K for the filling CV-3 of the mixture with $x_{GBL}=0.25$. The data obtained at the same state point for different fillings were averaged arithmetically since the individual uncertainties were comparable and all corresponding data agreed within uncertainties.

3 Results and Discussion

In the following, aspects related to sample stability during the different measurement series are addressed before the experimental results for interfacial tension and liquid dynamic viscosity of GBL, BDO, and their binary mixtures obtained by SLS, PD and CV are presented and discussed.

3.1 Analysis of Sample Stability

Considering the observed changes in the sample characteristics at $T>398$ K in a previous study regarding thermal and mass diffusivity of the GBL/BDO system performed by dynamic light scattering (DLS) from the liquid bulk of the fluid [49], special care was taken to ensure that σ and η_L data reported here are not influenced by such effects.

In the SLS experiments performed at approximately 0.1 MPa under H_2 atmosphere, the corresponding general strategy relies on frequent repetition measurements. The measurement procedure begins at a low T between (298 and 323) K, followed by a measurement at a larger T and a subsequent repetition measurement at a previously studied lower T. When agreement of the obtained data was found, the sample was studied at the next higher T, followed by another repetition measurement at a lower T. This procedure was repeated until the previously measured data could no longer be reproduced. In some cases, the measurement cell was cleaned and filled with a new sample for further check measurements.

For pure BDO, the measurement series performed with two fillings of the SLS sample cell were fully reproducible up to 473 K, i.e., the η_L and σ values obtained at the same T always agreed within combined uncertainties. In contrast, the data from the repetition measurements for GBL and the mixtures exhibited significant deviations from the initial ones after T had exceeded approximately 348 K. Beyond this point, also color changes of the sample were observed, which is represented by a change of the initial green color of the laser beam crossing these liquid samples at T up to 373 K to yellow at 423 K and eventually orange at 473 K as shown for the mixture with $x_{GBL} = 0.25$ in Fig. S1 in section S2 of the Supplementary Information.

To give an example of how the measured properties changed as soon as the sample composition was obviously altered, corresponding data are summarized for the mixture with $x_{GBL} = 0.25$. For this composition, the following three independent fillings of the SLS cell helped to analyze the stability aspect. During the first filling SLS-1 contributing to the data summarized in Sect. 3.2, measurements were performed over the T range from (298 to 398) K. For the fillings SLS-3 and SLS-4 that only served for studying the stability behavior, the first measurement at 373 K gave the same results although a comparison of the results of subsequent check measurements at lower T with the validated data from the filling SLS-1 indicated already a change of the sample at this T. From this starting point at 373 K, the samples were exposed to progressively higher maximum T, and repetitive SLS measurements were performed at 373 K afterward. The maximum T reached were 398 K for the filling SLS-1 as well as (423 and 473) K for the additional fillings SLS-3 and SLS-4. For the three fillings, the η_L values obtained from the repetition measurements at 373 K showed systematic increases of approximately (10, 14, and 24)% after prior exposure to (398, 423, and 473) K, respectively. Yet, the SLS measurements did not indicate any significant change in the simultaneously determined σ values for this mixture. For mixtures with $x_{GBL} = 0.75$ studied in a similar series of experiments, however, the obtained η_L data were hardly affected after exposure to larger T up to 473 K, but repetition measurements at 373 K resulted in clearly decreasing σ values. Mixtures with $x_{GBL} = 0.50$ were only studied up to 373 K by SLS, since after that, repetition measurements at 323 K showed changes of about −15% in η_L and −11% in σ. All corresponding data related to these observations are listed in Table S4.

Since SLS is highly sensitive to effects that may alter the dynamics of surface fluctuations, additional measurements with the LTCV setup were performed to check whether the change in η_L observed in the SLS data is related to formed impurities influencing the surface dynamics analyzed or whether they originate from changes of the bulk liquid. After cooling to room T, samples of the mixture with $x_{GBL} = 0.25$ taken from the used fillings SLS-3 and SLS-4 were measured. For the sample from the filling SLS-3, η_L measurements were performed at (298, 303, 323, and 348) K, while for the sample from the filling SLS-4, measurements were carried out at (303, 323, and 348) K. The η_L values obtained for these samples show pronounced deviations from those of a freshly prepared sample, where a systematic dependence on the prior thermal history was observed. The data given in Table S4 show that η_L measured for the sample from the filling SLS-3 was about (20 to 30)% larger from (298 to 348) K compared to the corresponding data for the fresh sample,

while these positive deviations were about (34 to 50)% from (303 to 348) K for the sample taken from the filling SLS-4. The increasing deviations with increasing maximum T to which the sample was exposed during the SLS measurement series hint at related changes in the sample composition. In addition, samples taken out from the SLS cell of these three fillings were checked in the PD setup at $T = 373$ K, where the deviations from the corresponding experimental PD data measured with fresh samples at this T were within 2% and, thus, agree with the observations related to the SLS measurements. These data are also given in Table S4.

In contrast to the behavior described in connection with the SLS measurements, GBL remained stable up to 473 K during HTCV measurements of a freshly prepared sample. The corresponding η_L data were reproducible in a measurement series with the same GBL sample corresponding to T of (348, 398, 348, 423, 348, 448, 348, 473, and 348) K. Consistent results were also obtained when the sample was kept at a given T for 2 h before measurement. In contrast, the three mixtures exhibited systematic increases in flow time during the measurement series at a given elevated T. These changes occurred for the first time at $T = 398$ K for the mixtures with $x_{GBL} = (0.25$ and $0.75)$ and at $T = 373$ K for the mixture with $x_{GBL} = 0.50$ and became more pronounced with increasing T. Detailed data related to these experiments by LTCV are provided in Table S5 of the Supplementary Information.

Applying the PD method for freshly prepared samples, it was observed at $T > 398$ K that after a certain residence time of a droplet hanging on the capillary tip, the liquid started to wet the outer capillary wall. This limited the time available for T equilibration of the formed droplet and for taking droplet images that can be analyzed properly regarding σ. While the observed alteration of the wetting behavior indicates a change of the sample composition, it will be shown in Sect. 3.2 that the σ values obtained from the analysis of the images taken before are rather consistent with the trends derived from the data determined at lower T.

To further analyze any changes in the samples during the SLS measurements, the Raman spectra recorded on the SLS setup were checked. Applying the procedure given in Sect. 2.3 and directly comparing the intensity ratios I_r obtained in this work at 323 K with the reference I_r values reported in Ref. [49], it is confirmed that the PDRS method applied here allows to determine the composition of the filled GBL/BDO mixtures. The corresponding data from the present study are provided in Table S6 of the Supplementary Information. With respect to potential changes in sample composition owing to, e.g., the formation of further compounds, representative example spectra are given in Fig. 3. It depicts the normalized isotropic spectra obtained for the mixture with $x_{GBL} = 0.25$ at $T = 373$ K when this T was studied for the first time for the filling SLS-1 and when the sample was cooled down to this T after it had been investigated at (398, 423, and 473) K for the fillings SLS-1, SLS-3, and SLS-4, respectively. The comparison shows that the selected peak areas related to GBL have decreased in the latter spectra, which is increasingly pronounced with increasing maximum T studied. In the same manner, a new peak increasingly appears at a Raman shift of about 1720 cm^{-1}. Although it could not be identified to which specific molecular vibrations this peak can be related, these observations seem to confirm that changes in the mixture composition have occurred. For the GBL/BDO system, different respective reactions are proposed in the literature. For example, 4-hydroxybutyl 4-hydroxybutanoate can be formed by the combination of GBL and BDO

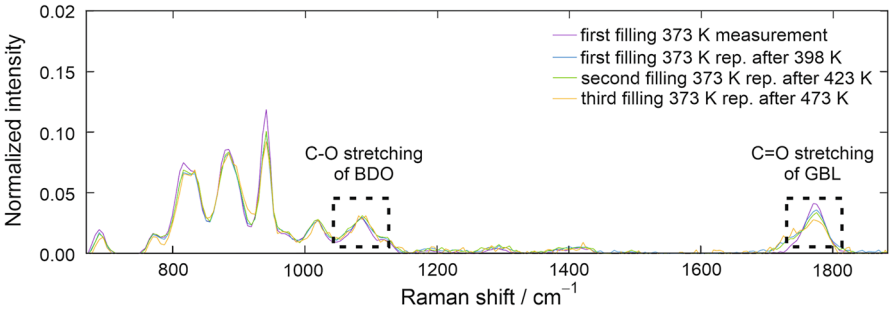


Fig. 3 Isotropic Raman spectra as a function of the Raman shift obtained in the liquid phase for three fillings of the mixture with $x_{GBL}=0.25$ within the SLS setup at $T \approx 373$ K. The dashed rectangles highlight the characteristic vibration modes for GBL at around 1760 cm^{-1} and for BDO at around 1085 cm^{-1}. Refer to the online version to distinguish between the different spectra by color

[27, 28, 76], which may be related to the limited T range accessible for their binary mixtures. Furthermore, tetrahydrofuran can be formed as a dehydration product of BDO [77, 78], which may become most relevant here at high T. Such reactions are associated with the formation of water, which could explain the rather high water content of the samples measured after SLS experiments despite the efforts to avoid the uptake of humidity from ambient air. Differences in the composition stability during the measurements by the different methods might be related to the different atmospheres, residence times of the samples in the setups, the duration of exposure to elevated T, and the different solid materials being in contact with the LOHC samples. A more detailed analysis of such connections is not in the scope of the present study and requires specialized investigations.

Based on these findings, T ranges in which the measured properties are considered to be reliable were determined for each technique and system. With SLS, reliable results were obtained from (298 to 473) K for BDO. For GBL and for the mixtures with $x_{GBL}=$(0.25 and 0.75), the corresponding T range is from (298 to 348) K, while it is limited to (298 to 323) K for $x_{GBL}=0.50$. In CV measurements, BDO and GBL were thermally stable up to 473 K. For the mixtures, reliable measurements could be performed up to 373 K for $x_{GBL}=$(0.25 and 0.75) and up to 348 K for $x_{GBL}=0.50$. Results from PD are considered to be fully reliable up to 398 K for all systems studied. In diagrams shown in the following, symbols with solid boundaries indicate measurement results that are reliably related to the given sample composition. Further data that are integrated in the discussion of the measurement results, but probably influenced with respect to sample composition, are represented by symbols with broken boundaries and marked with an asterisk in corresponding tables. Correlations developed by using solely the reliable measurement results are given by solid lines, while their extrapolation outside the respective T range is indicated by dashed lines.

3.2 Interfacial Tension

The experimental results for the interfacial tension σ of GBL, BDO, and their binary mixtures determined up to $T=473$ K at $p \approx 0.1$ MPa in a H_2 atmosphere are

Table 3 Interfacial tension σ and simultaneously measured liquid dynamic viscosity η_L from SLS under H_2 atmosphere at $p \approx 0.1$ MPa. Additionally, calculated values for ρ_L, ρ_G, and η_G used as input for the data evaluation according to section S1 are included[a]

T / K	Fillings used	ρ_L / (kg·m^{-3})[a]	ρ_G / (kg·m^{-3})[a]	η_G / (μPa·s)[a]	η_L / (mPa·s)	100 · $U_r(\eta_L)$	σ / (mN·m^{-1})	100 · $U_r(\sigma)$
GBL								
298.15 ± 0.09	SLS-3	1124.35	0.13	9.35	1.710	3.3	42.7	3.6
303.17 ± 0.03	SLS-3	1119.41	0.13	9.46	1.555	2.2	42.00	0.95
323.15 ± 0.06	SLS-1, -3	1099.76	0.15	9.97	1.197	2.4	39.20	1.7
348.16 ± 0.10	SLS-2, -3	1075.16	0.16	11.00	0.970	3.5	35.6	3.1
BDO								
298.16 ± 0.08[b]	SLS-1	1012.55	0.14	9.30	72.6	1.8	45.07[b]	2.0
303.20 ± 0.07[b]	SLS-1	1009.50	0.14	9.39	57.12	0.67	44.68[b]	2.0
323.15 ± 0.03[b]	SLS-1	997.33	0.14	9.75	24.00	1.3	43.13[b]	2.0
348.12 ± 0.06[b]	SLS-1	981.75	0.14	10.22	10.74	1.8	41.18[b]	2.0
373.14 ± 0.06	SLS-1	965.49	0.15	10.88	4.23	2.7	37.68	2.6
398.16 ± 0.06	SLS-1	948.30	0.17	12.20	2.56	4.9	35.60	2.0
423.15 ± 0.06	SLS-1	929.96	0.27	14.81	1.461	2.5	30.76	1.1
448.16 ± 0.06	SLS-1	910.14	0.52	13.35	0.984	2.1	27.74	1.6
473.16 ± 0.06	SLS-2	888.60	1.06	21.13	0.788	2.8	26.79	2.5
$x_{GBL} = 0.25$								
298.14 ± 0.05[b]	SLS-1	1039.25	0.11	9.31	22.40	1.7	44.89[b]	2.0
303.13 ± 0.06[b]	SLS-1	1035.70	0.11	9.41	18.73	1.6	44.43[b]	2.0
323.13 ± 0.06	SLS-1	1021.32	0.11	9.83	8.85	7.7	41.1	15
348.15 ± 0.07	SLS-1, -2	1002.93	0.13	10.48	4.081	2.4	37.80	2.2
$x_{GBL} = 0.50$								
298.17 ± 0.03	SLS-1	1063.16	0.13	9.32	8.14	3.9	43.4	6.5
303.17 ± 0.07	SLS-1	1059.14	0.13	9.43	7.05	4.3	43.39	1.7
323.16 ± 0.07	SLS-1, -2	1042.95	0.14	9.88	4.01	7.2	40.1	2.7
$x_{GBL} = 0.75$								
298.18 ± 0.06	SLS-1	1091.57	0.11	9.35	2.91	4.9	41.20	1.8
303.11 ± 0.08	SLS-1	1087.16	0.11	9.45	2.686	1.9	40.77	2.2
323.15 ± 0.04	SLS-1	1069.13	0.12	9.96	1.861	1.5	39.39	1.8
348.12 ± 0.06	SLS-1, -2	1046.43	0.14	10.91	1.292	2.7	34.59	2.2

[a]The ρ_L data were taken from Ref. [49], while the relative uncertainties for the input data $Ur(\rho_L)$, $Ur(\rho_G)$, and $Ur(\eta_G)$ are described in section S1 of the Supplementary Information. All uncertainties are given on a confidence level of 0.95 ($k = 2$)

[b]State points are related to the overdamped regime of surface fluctuations, where the given σ values from the correlation according to Eq. (8) based on the PD measurements are used as input for the evaluation of the SLS experiments to obtain η_L

summarized together with the corresponding η_L data in Table 3, while those obtained by PD are given in Table 4. No σ data from SLS are given for BDO and the mixture with $x_{GBL} = 0.25$ in the regime of low T due to an overdamped behavior of the surface waves. Because of this and since the experimental PD data considered to be reliable with respect to sample composition stability cover a broader T range than the respective SLS data, the PD data were used for establishing correlations of σ with respect to T according to

Table 4 Interfacial tension σ from the PD method as a function of T under H_2 atmosphere at $p \approx 0.1$ MPa. Additionally, calculated values for ρ_L and ρ_G used as input for the data evaluation are included[a,b]

T / K	Fillings used	ρ_L / (kg·m^{-3})[a]	ρ_G / (kg·m^{-3})[a]	σ / (mN·m^{-1})[a]	T / K	Fillings used	ρ_L / (kg·m^{-3})[a]	ρ_G / (kg·m^{-3})[a]	σ / (mN·m^{-1})[a,b]
GBL									
296.15 ± 0.19	PD-2	1120.67	0.08	44.97	373.18 ± 0.09	PD-1, -2	1044.62	0.19	34.79
298.53 ± 0.47	PD-1	1118.35	0.09	43.89	398.21 ± 0.05	PD-1, -2	1019.54	0.36	31.79
303.12 ± 0.05	PD-1, -2	1113.86	0.09	43.12	423.28 ± 0.07*	PD-1–3	994.22	0.73	28.60*
323.21 ± 0.05	PD-1, -2	1094.16	0.11	40.23	448.15 ± 0.08*	PD-2, -3	968.92	1.50	25.84*
348.24 ± 0.05	PD-1, -2	1069.44	0.12	38.06	473.15 ± 0.07*	PD-2, -3	943.30	2.91	23.35*
BDO									
295.16 ± 0.04	PD-1	1014.36	0.09	45.17	398.05 ± 0.11	PD-2	948.38	0.34	37.00
303.18 ± 0.04	PD-1, -2	1009.51	0.09	44.74	423.20 ± 0.11*	PD-2, -3	929.92	0.72	34.23*
323.16 ± 0.04	PD-1, -2	997.32	0.08	43.25	448.20 ± 0.05*	PD-2, -3	910.10	1.47	31.62*
348.14 ± 0.06	PD-1, -2	981.74	0.15	40.89	473.68 ± 0.19*	PD-3	888.13	2.82	28.66*
373.13 ± 0.07	PD-1, -2	965.48	0.18	39.75					
$x_{GBL} = 0.25$									
293.37 ± 0.05	PD-1	1042.62	0.09	45.12	398.18 ± 0.13	PD-1	964.79	0.36	35.46
303.19 ± 0.06	PD-1	1035.67	0.09	44.50	423.15 ± 0.15*	PD-1	945.10	0.75	32.57*
323.16 ± 0.08	PD-1	1021.30	0.10	42.57	448.31 ± 0.18*	PD-1	924.79	1.53	29.79*
348.19 ± 0.13	PD-1	1002.90	0.13	40.53	473.19 ± 0.20*	PD-1	904.28	2.97	27.37*
373.16 ± 0.08	PD-1	984.09	0.19	38.07					
$x_{GBL} = 0.50$									
295.80 ± 0.12	PD-1	1065.06	0.10	44.46	398.18 ± 0.10	PD-1	980.48	0.36	34.47
303.10 ± 0.05	PD-1	1059.20	0.10	43.47	423.32 ± 0.04*	PD-1	958.94	0.36	31.59*
323.10 ± 0.17	PD-1	1043.00	0.11	41.79	448.36 ± 0.08*	PD-1	937.20	0.75	28.72*
348.21 ± 0.06	PD-1	1022.39	0.13	39.96	473.19 ± 0.14*	PD-1	915.34	1.53	26.29*
373.16 ± 0.08	PD-1	1001.61	0.22	37.23					
$x_{GBL} = 0.75$									
296.26 ± 0.05	PD-1	1093.29	0.11	43.74	398.08 ± 0.08	PD-1	1000.34	0.36	32.39
303.19 ± 0.25	PD-1	1087.09	0.11	43.07	423.12 ± 0.16*	PD-1, -2	976.89	0.73	29.52*
323.12 ± 0.04	PD-1	1069.15	0.11	41.07	448.07 ± 0.09*	PD-1, -2	953.29	1.49	27.05*
348.13 ± 0.10	PD-1	1046.42	0.11	38.34	472.91 ± 0.09*	PD-1, -2	929.56	2.88	24.76*
373.04 ± 0.10	PD-1	1023.57	0.18	35.42					

[a]The relative uncertainty for the measured σ values is $U_r(\sigma) = 2\%$ for $T \leq 398$ K and $U_r(\sigma) = 3\%$ for $T > 398$ K. The relative uncertainties for the input data $U_r(\rho_L)$ and $U_r(\rho_G)$ are described in section S1 of the Supplementary Information. All uncertainties are given on a confidence level of 0.95 ($k = 2$)

[b]Data that need to be handled with care owing to slight instabilities are marked with an asterisk (*)

$$\sigma_{calc}(T) = \sigma_0 + \sigma_1 T. \tag{8}$$

In the least-squares minimization algorithm applied for the fitting procedure, all data points for σ were considered with the same statistical weight. The fitting parameters σ_0 and σ_1 are listed in Table 5 together with the average absolute relative deviations (AARDs) of the measured data from the correlation. The relative deviations of the experimental PD data from Eq. (8) are always within their expanded uncertainty.

Table 5 Coefficients of Eq. (8) for the calculation of the interfacial tension σ_{calc} of the systems studied, determined with the experimental σ data obtained by PD at $T \leq 398$ K

Sample	σ_0 / (mN·m^{-1})	σ_1 / (mN·m^{-1}·K^{-1})	AARD / %[a]
GBL	79.165	−0.11890	0.82
BDO	68.315	−0.07795	0.61
$x_{GBL}=0.25$	72.355	−0.09213	0.36
$x_{GBL}=0.50$	72.453	−0.09469	0.53
$x_{GBL}=0.75$	76.870	−0.11127	0.36

[a]Average absolute relative deviation of the experimental data from the corresponding fits

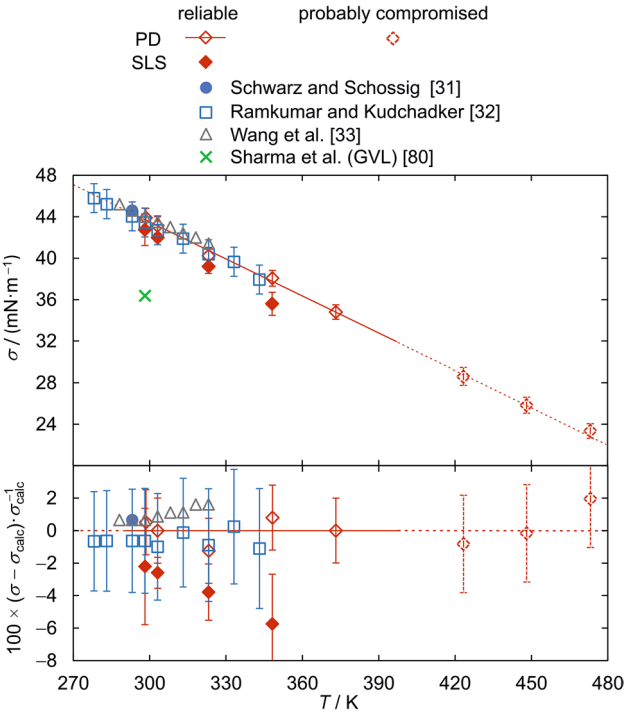


Fig. 4 Experimental σ data of GBL as a function of T at $p \approx 0.1$ MPa in H_2 atmosphere together with the literature data available for this substance [31–33] and literature data for the structurally related compound GVL [80]. The upper part shows the absolute values, while the lower part shows the relative deviations from the correlation of data from PD according to Eq. (8). The dashed line indicates the extrapolation of the correlation beyond the T range considered for its determination

This can be seen in the lower parts of following figures, where the correlations serve as a reference in deviation plots.

Figures 4 and 5 depict the T dependency of the experimental σ data for pure GBL and BDO obtained in the present work by PD and SLS measurements and from the literature as well as their relative deviations from the corresponding correlations based on Eq. (8).

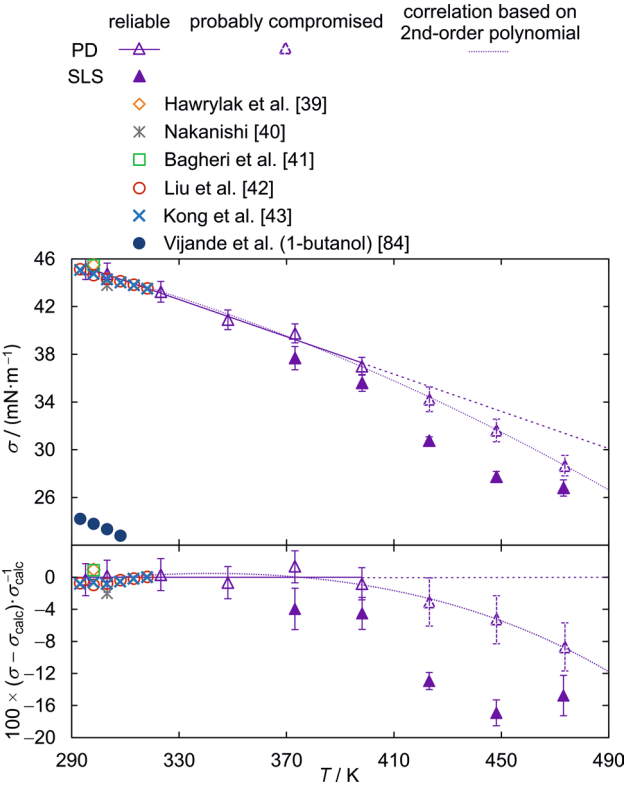


Fig. 5 Experimental σ data of BDO as a function of T at $p \approx 0.1$ MPa in H_2 atmosphere together with the corresponding literature data [39–43, 84]. The upper part shows the absolute values, while the lower part shows the relative deviations from the correlation of data from PD according to Eq. (8). The dashed line indicates the extrapolation of the correlation beyond the T range considered for its determination. The dotted line represents a fit of all PD data based on a polynomial of second order

For GBL, the σ data measured by PD and given in Fig. 4 indicate a rather large interfacial tension of this polar substance and the expected decrease with increasing T. The extrapolation of the correlation to larger T captures the PD data determined from droplet images recorded before the wetting of the outer cannula wall occurred with a maximum deviation of 1.2%. The σ values obtained from SLS agree with the PD results within their combined uncertainties at $T \leq 323$ K. In this range, SLS yields values that are approximately (2 to 4)% lower than corresponding PD data, which is consistent with observations reported in previous studies [9, 55]. At $T = 348$ K, the value from SLS exhibits a deviation of −5.7% relative to the PD-based correlation, which is slightly outside combined uncertainties. This could be interpreted as an indication of the onset of changes in the sample composition in the SLS cell before no more reproducible results could be obtained at larger T. The increasing deviations may be explained by the fact that with SLS, σ is determined from the analysis of the dynamics of surface fluctuations. The technique

is therefore sensitive to small amounts of weakly surface-active species that modify the interfacial rheology, whereas the PD method probes a quasi-static equilibrium condition. Similar phenomena have been reported by Koller et al. [79], who showed that weak surfactants can cause an apparent reduction of σ values measured in SLS. Thus, the more pronounced deviation of the SLS from the PD data observed at $T = 348$ K for GBL may indicate the beginning formation of small amounts of surface-active species, possibly related to the onset of thermal degradation at that T and, in a more pronounced manner, at larger T. Such species would primarily influence the interfacial dynamics probed by SLS, whereas the quasi-static PD measurements remain essentially unaffected. Such sensitivity also implies that even trace impurities may introduce measurable effects.

The available literature data for GBL from Refs. [31–33] are consistent with σ_{calc} within the experimental uncertainty. For the value at $T = 293$ K from Ref. [31], no details on the measurement method or associated uncertainty is reported. In contrast, the data from Ramkumar and Kudchadker [32] were measured with the capillary rise method and a stated accuracy of $\pm 1.4 \cdot 10^{-3}$ N·m^{-1}, while those obtained by Wang et al. [33] with a platinum plate method are reported to exhibit an accuracy of ± 0.1 mJ·m^{-2}. Due to the small amount of literature data available for GBL, an additional comparison is made with γ-valerolactone (GVL) [80], which exhibits the same lactone ring structure, but with an additional methyl group attached to the ring. At $T = 298$ K, the reported σ of GVL is 17% smaller than σ_{calc} for GBL, showing that the additional methyl group seems to have a significant influence on σ of the γ-lactones.

For BDO, Fig. 5 shows that σ measured by PD tends to decrease linearly with increasing T in the range where wetting of the outer capillary did not occur. In contrast to GBL, the corresponding data at larger T exhibit a more pronounced decrease, resulting in a deviation of −9% from the extrapolated correlation according to Eq. (8). This behavior could be captured better with a polynomial of second order as indicated by the dashed line representing such a fit equation by considering all PD data. Such behavior is typical for fluids with strong hydrogen bonding such as water [81] or 2-propanol [75] and, thus, also plausible for this diol. The strength of such bonding in BDO can be rationalized by comparison with 1-butanol, where at $T = 298$ K, σ for BDO is by a factor of 1.9 larger than that of its counterpart with only one hydroxyl group [82].

For $T = (373$ and $398)$ K, the results from SLS in the damped oscillatory regime of surface fluctuations agree with the PD data with deviations of approximately −4%. For larger T, however, more pronounced deviations of about −15% are observed although the repetition measurements in the SLS experiments at lower T did not indicate any significant changes in sample composition. This may be explained partially by increasing uncertainties in the PD measurements at elevated T due to the onset of capillary wetting and enhanced evaporation. For SLS, on the other hand, small amounts of formed impurities might influence the surface fluctuations that become more intense at larger T.

All available reference data sets from the literature for BDO cover a limited T range from (293 to 318) K. Du Nouy ring tensiometers were employed by Hawrylak et al. [39] and Bagheri et al. [41]. Hawrylak et al. stated an accuracy of about

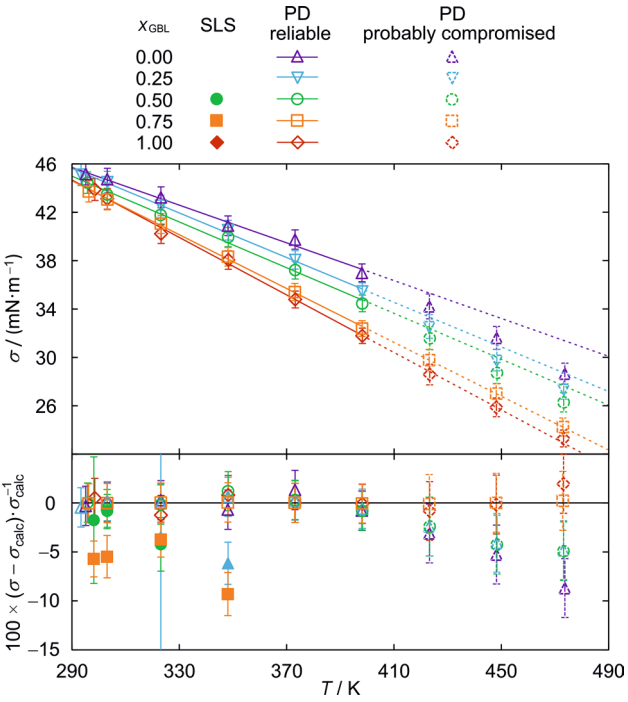


Fig. 6 Experimental σ data of the five investigated systems as a function of T at $p \approx 0.1$ MPa in H_2 atmosphere obtained by PD and SLS. The upper part shows the absolute PD data together with their corresponding T-dependent correlations according to Eq. (8). The lower part shows the relative deviations of the SLS data for the mixtures and all experimental PD data from these correlations

± 0.20 mN·m^{-1}, while Bagheri et al. claimed an uncertainty of ± 0.20 mN·m^{-1} with a reproducibility of ± 0.01 mN·m^{-1}. Nakanishi [40] applied the capillary rise method and stated an estimated accuracy of ± 0.3 mN·m^{-1}. Liu et al. [42] performed measurements with a surface tensiometer calibrated using water and ethanol. Although the measurement principle used was not specified, an error range of ± 0.3 mN·m^{-1} was claimed based on repeated measurements. Kong et al. [43] measured σ in the same T range from (293.15 to 318.15) K using an automatic surface tension meter based on the Wilhelmy platinum plate method, with a stated error of ± 0.03 mN m^{-1}. Figure 5 shows that all literature data agree with the present PD measurements within 2%.

σ of pure GBL and BDO is compared with the data for the binary mixtures in Fig. 6, where no literature data for the latter could be found. As the absolute deviations between the data for the different systems and measurement methods are small, only PD data are shown in the upper part of the figure to improve readability. In the lower part, the SLS data for the mixtures (filled symbols) and all PD data (open symbols) are plotted in terms of their relative deviations from the respective PD-based correlations.

The results obtained by PD and SLS all exhibit a linear decrease of σ with increasing T up to 398 K within the respective sample stability limits. As visible in the lower part of Fig. 6, the deviation from this behavior at larger T discussed for BDO is less pronounced for the mixtures. The upper part of Fig. 6 additionally shows that at a given T, σ decreases systematically with increasing x_{GBL}. Considering the measurement uncertainties and the small differences between σ of the pure mixture components, any conclusion regarding possible mixing rules with respect to σ would be speculative and are therefore not addressed here.

The lower part of Fig. 6 illustrates that for the mixtures, the σ data from SLS considered to be reliable in the limited T range up to (323 and 348) K deviate in a very similar manner from the corresponding PD data as those for pure GBL. This includes negative deviations that are less than 6% and within combined uncertainties up to $T = 323$ K, while somewhat larger negative deviations of up to about 10% are found at $T = 348$ K. The fact that this behavior occurs consistently across several compositions suggests a systematic effect rather than random scatter. Here, the possible onset of sample composition changes and their impact on the analyzed surface fluctuations already discussed in detail in connection with the SLS data for pure GBL may apply as well. This interpretation is speculative, but offers a reasonable explanation for the systematic deviations found for GBL-containing samples, which nevertheless remain moderate.

3.3 Liquid Viscosity

The experimental results for the liquid dynamic viscosity η_L of GBL, BDO, and their binary mixtures determined by SLS at T up to 473 K at $p \approx 0.1$ MPa in a H_2 atmosphere are given in Table 3. The values reported for the overdamped case of surface fluctuations were determined by using the σ values from the correlation according to Eq. (8). Table 6 provides the η_L values calculated from the ν_L data measured by CV. The CV measurements were carried out in ambient air at T up to 348 K in the LTCV setup and under an Ar atmosphere from (348 to 473) K in the HTCV. Both tables also show the input data used for data evaluation. Because of the same reasons as for σ, the CV data were used for establishing correlations for η_L as a function of T according to

$$\eta_{L,calc} = \eta_{L,0} \cdot \exp\left(\sum_{i=1}^{n} \frac{\eta_{L,i}}{T^i}\right), \tag{9}$$

where $n = 3$ for the mixture with $x_{GBL} = 0.25$ and $n = 2$ otherwise. To determine the fit parameters $\eta_{L,0}$, $\eta_{L,1}$, $\eta_{L,2}$, and $\eta_{L,3}$ in Eq. (9), the natural logarithm of the η_L values in units of mPa·s were correlated as a function of $(T/K)^{-1}$. All data points were assigned equal statistical weight, and the parameters were obtained through a least-squares deviation minimization procedure. The fit parameters and the AARDs of the measured η_L from $\eta_{L,calc}$ are listed in Table 7. In all cases, Eq. (9) reproduces the experimental CV data within their expanded ($k = 2$) uncertainties.

Table 6 Liquid dynamic viscosity η_L obtained by CV at $p = 0.1$ MPa at atmospheric conditions or under an Ar atmosphere as a function of T. Additionally, calculated values for ρ_L used as input for the evaluation according to section S1 of the Supplementary Information are included

T / K	Fillings used[a]	ρ_L / (kg·m^{-3})[a]	η_L / (mPa·s)	100 · $U_r(\eta_L)$	T / K	Fillings used[a]	ρ_L / (kg·m^{-3})[a]	η_L / (mPa·s)	100 · $U_r(\eta_L)$
GBL									
298.20 ± 0.04	CV-1, -2	1124.30	1.714	0.78	398.17 ± 0.04	CV-3, -4	1025.48	0.5665	0.83
303.19 ± 0.05	CV-1, -2	1119.39	1.592	0.91	423.24 ± 0.05	CV-3, -4	1000.14	0.4682	0.75
323.15 ± 0.03	CV-1, -2	1099.77	1.206	1.0	448.22 ± 0.05	CV-3	974.44	0.3947	0.69
348.13 ± 0.04	CV-1–4	1075.19	0.9012	0.92	472.86 ± 0.10	CV-3	948.56	0.3382	0.75
373.15 ± 0.05	CV-3	1050.45	0.7008	0.70					
BDO									
298.20 ± 0.04	CV-1	1012.52	69.80	0.84	398.21 ± 0.04	CV-2, -3	948.27	2.641	0.82
303.20 ± 0.04	CV-1	1009.49	54.96	0.72	423.21 ± 0.04	CV-2, -3	929.91	1.622	0.84
323.16 ± 0.04	CV-1	997.32	23.29	0.75	448.25 ± 0.12	CV-2, -3	910.07	1.0744	0.91
348.14 ± 0.04	CV-1, -2	981.73	9.794	0.88	472.93 ± 0.07	CV-2, -3	888.81	0.7620	0.92
373.16 ± 0.04	CV-2, -3	965.47	4.786	0.99					
$x_{GBL} = 0.25$									
298.19 ± 0.05	CV-1	1039.22	21.08	0.66	348.15 ± 0.05	CV-1, -2	1002.93	4.196	0.94
303.19 ± 0.05	CV-1	1035.66	17.24	0.68	373.13 ± 0.04	CV-2, -3	984.11	2.529	1.5
323.16 ± 0.03	CV-1	1021.30	8.506	0.67					
$x_{GBL} = 0.50$									
298.22 ± 0.05	CV-1	1063.12	8.252	0.71	323.21 ± 0.06	CV-1, -2	1042.91	4.002	0.86
303.21 ± 0.07	CV-1	1059.11	7.024	0.70	348.15 ± 0.10	CV-2	1022.44	2.280	0.66
$x_{GBL} = 0.75$									
298.19 ± 0.05	CV-2, -4	1093.80	3.221	0.72	348.15 ± 0.05	CV-1, -3	1046.41	1.2868	0.71
303.21 ± 0.06	CV-1, -2, -4	1087.07	2.882	0.71	373.16 ± 0.04	CV-3	1023.45	0.9327	1.0
323.19 ± 0.07	CV-1, -2	1069.08	1.922	0.79					

[a]The relative uncertainties for the input data $U_r(\rho_L)$ are described in section S1 of the Supplementary Information. All uncertainties are given on a confidence level of 0.95 ($k = 2$). Capillary 0 was used for the third and fourth fillings of GBL from (348 to 473) K. Capillary 0a was used for second filling of $x_{GBL} = 0.50$ from (323 to 348) K and the fourth filling of $x_{GBL} = 0.75$ from (298 to 303) K. Capillary 0c was used for the first and second fillings of GBL from (298 to 348) K, the second and third fillings of BDO from (398 to 473) K, the third filling of $x_{GBL} = 0.25$ at 373 K, and the first three fillings of $x_{GBL} = 0.75$ from (298 to 373) K. Capillary Ic was used for the first and second fillings of BDO from (323 to 373) K, the first and second fillings of $x_{GBL} = 0.25$ from (298 to 348) K, and the first filling of $x_{GBL} = 0.50$ from (298 to 323) K. Capillary IIc was used for the first filling of BDO from (298 to 303) K

Figures 7 and 8 show the T dependency of the experimental η_L results for GBL and BDO obtained in this work from CV and SLS measurements together with the available literature data in the same manner as previously given for σ.

For GBL, the upper part of Fig. 7 shows the expected decrease of η_L with increasing T. Up to $T = 323$ K, the η_L values obtained from SLS agree with the corresponding CV results within the uncertainties of the former. At $T = 348$ K, the η_L value determined

Table 7 Coefficients of Eq. (9) for the calculation of the liquid dynamic viscosity $\eta_{L,calc}$ of the studied systems, determined with the experimental η_L data from CV

Sample	$\eta_{L,0}$ / (mPa·s)	$\eta_{L,1}$ / K	$\eta_{L,2}$ / K^2	$\eta_{L,3}$ / K^3	T range / K	AARD / %[a]
GBL	2.68071×10^{-2}	1.13545×10^{2}	3.10036×10^{4}	–	298–473	0.29
BDO	2.21692×10^{-2}	4.24122×10^{2}	5.89836×10^{5}	–	298–473	0.27
$x_{GBL}=0.25$	6.80018×10^{-2}	-2.66277×10^{4}	8.97478×10^{6}	-8.89079×10^{8}	298–373	0.12
$x_{GBL}=0.50$	1.65372×10^{-2}	-5.94434×10^{2}	5.24962×10^{5}	–	298–348	0.04
$x_{GBL}=0.75$	1.69838×10^{-2}	-3.27799×10^{2}	3.59512×10^{5}	–	298–373	0.11

[a]Average absolute relative deviation of the experimental data from the corresponding fits

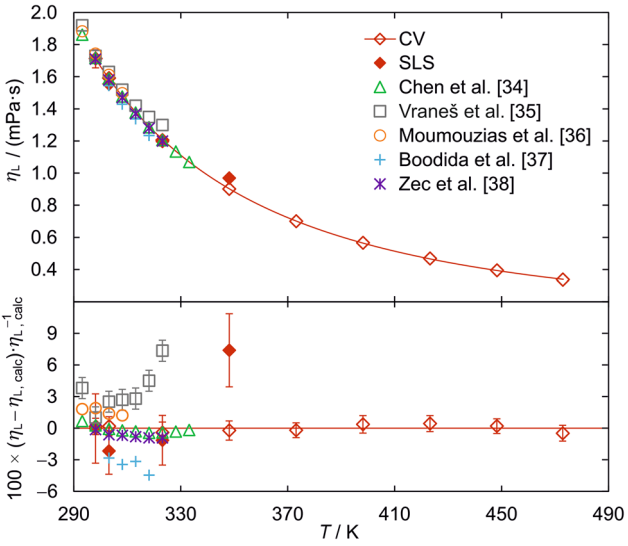


Fig. 7 Experimental η_L data of GBL obtained by CV and SLS as a function of T at $p \approx 0.1$ MPa together with the corresponding literature data [34–38]. The upper part shows the absolute values, while the lower part shows the relative deviations from the correlation of data from CV according to Eq. (9)

by SLS exhibits a deviation of +7.4% relative to the CV-based correlation according to Eq. (9). This behavior is similar to that observed for σ, where the respective explanations also apply here. The deviation plot in the lower part of Fig. 7 shows that most of the literature data covering a T range from (293 to 333) K agree well with the corresponding CV measurements. This is particularly true for the data from Chen et al. [34] obtained by rolling-ball viscometry and Zec et al. [38] measured by CV with Ubbelohde viscometers, where the deviations from Eq. (9) are less than 1% and, thus, within combined uncertainties. The data from Moumouzias et al. [36] determined by CV are approximately 2% larger than those from Eq. (9), while the reported reproducibility in viscosity was better than 0.2%. The values reported by Boodida et al. [37], measured using CV with a stated uncertainty of 0.005 mPa·s, exhibit corresponding deviations of around 3%. The largest deviations of up to 7.3% from the present correlation are

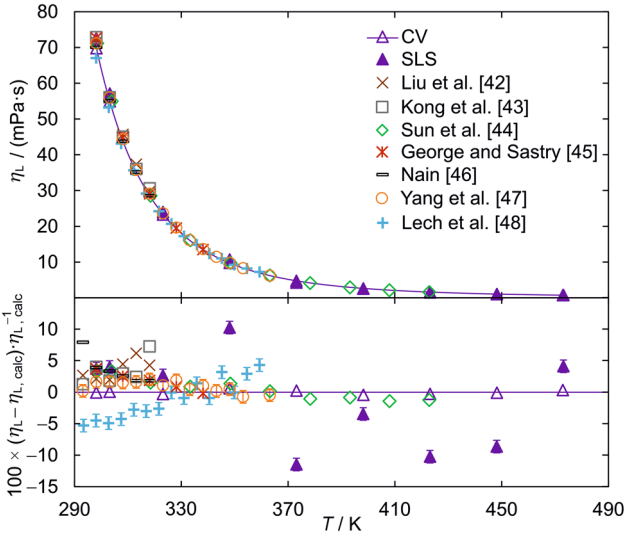


Fig. 8 Experimental η_L data of BDO obtained by CV and SLS as a function of T at $p \approx 0.1$ MPa together with the corresponding literature data [42–48]. The upper part shows the absolute values, while the lower part shows the relative deviations from the correlation of data from CV according to Eq. (9)

given for the data of Vraneš et al. [35]. These were obtained by rotational viscometry with a stated uncertainty of about 1%. The viscometer cell was equipped with a compartment intended to protect the sample from moisture, and the water content was determined prior to the measurements, while no information on the water content after the experiments is provided. Overall, the new results presented agree reasonably with the literature data and distinctly expand the T range covered previously.

For BDO, Fig. 8 shows that at T up to 323 K, the η_L values obtained from SLS agree with the CV results within approximately 4%. This T range is related to the overdamped regime of surface fluctuations, where σ values from the correlation according to Eq. (8) based on the PD measurements were used as input for the evaluation of the SLS experiments to obtain η_L. The observed agreement is reasonable, considering the individual uncertainties associated with SLS, PD, and CV experiments. At T from (348 to 373) K, the SLS signal transitions from the overdamped regime to the damped oscillatory regime. Since this T range is close to the critical damping, where $Y \approx 0.145$, a second exponential mode with significant amplitude and a decay time similar to that of the primary mode contributes to the signal, thereby making the fitting more difficult and increasing the uncertainty. Under such conditions, the commonly used first-order approximation for the evaluation of the CF may no longer provide a fully reliable description of the signal dynamics as discussed in Ref. [83]. Consequently, the uncertainties in the derived η_L values may be underestimated, which can explain the deviations on the order of −(5 to 10)% from the CV data. For T=(423 and 448) K, deviations of the SLS data from those from CV of around −10% are observed. Repeated measurements performed in both setups reproduced the original values well, and no signs of thermal degradation were detected

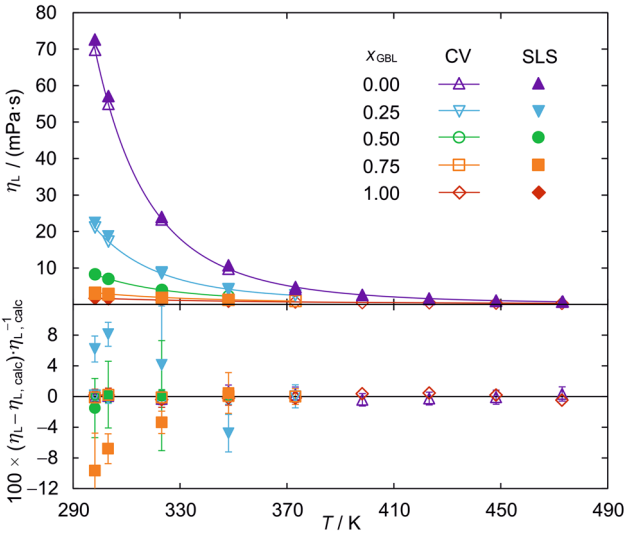


Fig. 9 Experimental η_L data of the five systems investigated as a function of T at $p \approx 0.1$ MPa obtained by CV and SLS. The upper part shows the absolute measurement values for SLS and CV together with their corresponding correlations based on CV data. The lower part shows the relative deviations of the SLS data for the mixtures and of all experimental CV data from the correlation of the data from CV according to Eq. (9)

by means of check measurements at low T after studying large T. It may be speculated that although a constant T was measured along the whole capillary of the viscometer, T gradients in the upper region of the oil bath of the HTCV setup reaching down to the upper reservoir of the viscometer might influence T of the sample in the capillary and falsify the CV data. Yet, the good agreement of the SLS and CV data at $T = 473$ K contradicts this speculation. A further possible reason may be T-dependent influences of small impurities in the BDO samples on the SLS results.

The comparison in the lower part of Fig. 8 shows that most literature data agree with the present CV measurement results within approximately 5%. The corresponding studies were mainly performed with CV [42–47], while Lech et al. [48] used rotational viscometry. Only two data points exhibit noticeably larger deviations of (7.2 and 7.9)%, which are the value at $T = 318.15$ K reported by Kong et al. [43] and the value at $T = 293.15$ K reported by Nain [46]. In both cases, the corresponding data represent measurements at one of the boundaries of T-dependent series where all other data agree with the present CV data within about 3%.

The upper part of Fig. 9 depicts the T-dependent data of η_L additionally measured by CV and SLS for three binary mixtures of BDO and GBL together with the corresponding values for the pure components. For all systems, η_L decreases strongly with increasing T, following the expected exponential-type behavior that is characteristic of associating liquids [48, 84, 85]. Limitations with respect to the accessible T range for the mixtures have already been discussed in detail in Sect. 3.1. The figure depicts that at a given T, η_L is distinctly larger for BDO compared to GBL. This may be attributed to the two terminal hydroxyl groups of BDO, which promote strong intermolecular hydrogen

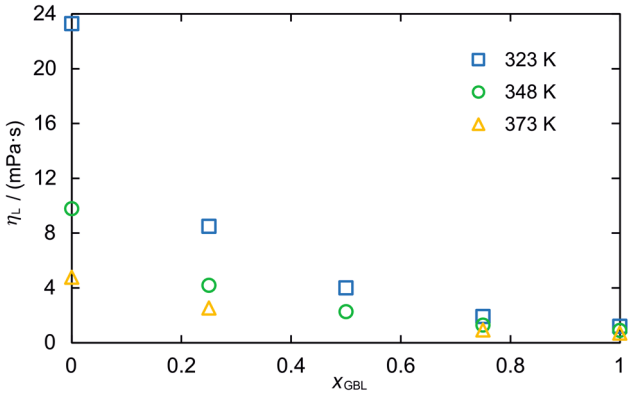


Fig. 10 Experimental η_L data from CV as a function of x_{GBL} for selected T

bonding and thereby increase the resistance to molecular motion. In contrast, the cyclic ester structure of GBL leads to weaker intermolecular interactions and thus lower η_L.

The lower part of Fig. 9 shows that for the mixtures, deviations between the data from SLS and CV remain moderate overall, but are most pronounced for the mixtures with x_{GBL}=(0.25 and 0.75) at low T. For the mixture with x_{GBL}=0.75, the relatively large deviations at T=(298 and 303) K may be attributed to the SLS signals being close to the critical damping regime, with $Y \approx$ (2.08 and 2.31), where the signal evaluation becomes increasingly sensitive to fitting uncertainties. For the mixture with x_{GBL}=0.25, the SLS measurements at T=(298 and 303) K correspond to the overdamped regime of surface fluctuations, as already discussed above for pure BDO. In this regime, PD-derived σ values are required as input for the evaluation, so that the corresponding uncertainties propagate into the resulting η_L. Together with the increased limitation for the signal analysis close to the critical damping, where $Y \approx 0.04$ at T=298 K and $Y \approx 0.05$ at T=303 K, this can explain the larger deviations between SLS and CV observed at these T.

The decrease of η_L with increasing x_{GBL} is illustrated in more detail in Fig. 10 based on CV results obtained in the T range where sample stability was given. The figure shows that adding GBL to BDO has a disproportionate influence on η_L, which has also been reported for other mixtures of associating liquids in which changes in intermolecular association upon mixing significantly influence the η_L behavior [86, 87]. In mixtures of alcohols with other hydrogen-bond-accepting components, such as the GBL/BDO system, self-association between alcohol molecules may be partially replaced by cross-association between the mixture components, which alters the hydrogen-bond structure of the liquid and affects η_L [86]. Similar interpretations have been reported for related associating mixtures where hydrogen-bond interactions govern the thermophysical behavior upon mixing [87].

4 Conclusions

In this work, σ and η_L of the LOHC compounds GBL and BDO as well as their binary mixtures were investigated over a broad T range up to 473 K using SLS, CV, and PD under gas atmospheres at $p \approx 0.1$ MPa. Particular attention was paid to the assessment of sample stability, which proved essential for identifying the reliably accessible T ranges for each method and sample composition. Using SLS under H_2 atmosphere, BDO remained stable up to 473 K. In contrast, irreversible changes could be observed starting from approximately 348 K for GBL and most mixtures as well as from 323 K for the mixture with $x_{GBL}=0.50$, partially indicated by changes found in the recorded Raman spectra. In CV measurements under Ar atmosphere, BDO and GBL were stable over the full T range up to 473 K, while the mixtures' characteristics started to change at $T=373$ K and, for $x_{GBL}=0.50$, already at around $T=348$ K. In PD experiments under H_2 atmosphere, increased wetting of the outer capillary wall was observed for all systems starting from $T=398$ K. Within these stability limits, the SLS data agree with those from CV and PD mostly within combined uncertainties. Expected limitations in this respect are given near the transition from the overdamped to the damped oscillatory regime of surface fluctuations probed by SLS. Further deviations could be related to the sensitivity of SLS to weakly surface-active trace impurities as well as slight T inhomogeneities in the oil bath for HTCV and evaporation effects at pendant drops at large T.

σ decreases nearly linearly with increasing T for all systems, while it follows a monotonic decrease with increasing x_{GBL} between the rather similar values for pure BDO and GBL. η_L is distinctly larger for pure BDO compared to GBL, which can be associated with the two terminal hydroxyl groups of BDO. For all systems, η_L shows an exponential decay with increasing T. For the mixtures, η_L is dominated by the contribution from the lower-viscosity component GBL, which may be related to the breaking of the strong hydrogen bonds between BDO molecules by cross-association with GBL.

This work distinctly expands the T range in which σ and η_L data are available for GBL and BDO and presents the first corresponding data sets for their binary mixtures. This provides a consistent basis for the modeling of hydrogenation/dehydrogenation processes in connection with the promising GBL/BDO LOHC system, thereby facilitating its further development into a technically viable H_2 storage technology.

Supplementary Information The online version contains supplementary material available at https://doi.org/10.1007/s10765-026-03808-5.

Acknowledgments The authors gratefully acknowledge funding of the Erlangen Graduate School in Advanced Optical Technologies (SAOT) by the Bavarian State Ministry for Science and Art.

Author Contributions The manuscript was written through contributions of all authors. All authors have given approval to the final version of the manuscript.

Funding Open Access funding enabled and organized by Projekt DEAL. This work was financially supported by the Bavarian Ministry of Economic Affairs, Regional Development and Energy as well as by the German Research Foundation (Deutsche Forschungsgemeinschaft, DFG) via the Project-ID 524349465.

Data Availability In addition to the data tables provided in the main paper, further data are given in the Supplementary Information (SI). While SI 1 provides further data tables, raw data related to the measurements in the present study are available in XLSX files. SI 2 contains the raw data from SLS. The raw data

for PD measurements are provided in a combined manner in SI 3. SI 4 contains the raw data from CV measurements, while the raw data from PDRS are provided in SI 5.

Declarations

Competing interest The authors declare no competing interests.

Open Access This article is licensed under a Creative Commons Attribution 4.0 International License, which permits use, sharing, adaptation, distribution and reproduction in any medium or format, as long as you give appropriate credit to the original author(s) and the source, provide a link to the Creative Commons licence, and indicate if changes were made. The images or other third party material in this article are included in the article's Creative Commons licence, unless indicated otherwise in a credit line to the material. If material is not included in the article's Creative Commons licence and your intended use is not permitted by statutory regulation or exceeds the permitted use, you will need to obtain permission directly from the copyright holder. To view a copy of this licence, visit http://creativecommons.org/licenses/by/4.0/.

References

1. V. Tietze, S. Luhr, D. Stolten, *Hydrogen Science and Engineering: Materials Systems and Technology* (Wiley-VCH Verlag, 2016), pp.659–689
2. B.G. Pollet, I. Staffell, J.L. Shang, Electrochim. Acta **84**, 235 (2012). https://doi.org/10.1016/j.electacta.2012.03.172
3. M.C. Massaro, R. Biga, A. Kolisnichenko, P. Marocco, A.H.A. Monteverde, M. Santarelli, J. Power. Sources **555**, 232397 (2023). https://doi.org/10.1016/j.jpowsour.2022.232397
4. P. Preuster, C. Papp, P. Wasserscheid, Acc. Chem. Res. **50**, 74 (2017). https://doi.org/10.1021/acs.accounts.6b00474
5. D. Teichmann, W. Arlt, P. Wasserscheid, R. Freymann, Energy Environ. Sci. **4**, 2767 (2011). https://doi.org/10.1039/c1ee01454d
6. D. Teichmann, W. Arlt, P. Wasserscheid, Int. J. Hydrogen Energy **37**, 18118 (2012). https://doi.org/10.1016/j.ijhydene.2012.08.066
7. P. Wasserscheid, Nat. Energy **10**, 924 (2025). https://doi.org/10.1038/s41560-025-01832-7
8. F. Alhumaidan, D. Cresswell, A. Garforth, Energy Fuels **25**, 4217 (2011). https://doi.org/10.1021/ef200829x
9. M. Kerscher, J.H. Jander, J. Cui, P. Wasserscheid, M.H. Rausch, T.M. Koller, A.P. Fröba, Int. J. Hydrogen Energy **48**, 29651 (2023). https://doi.org/10.1016/j.ijhydene.2023.04.103
10. P.S. Schmidt, M. Kerscher, T. Klein, J.H. Jander, F.E. Berger Bioucas, T. Rüde, S. Li, M. Stadelmaier, S. Hanyon, R.R. Fathalla, A. Bösmann, P. Preuster, P. Wasserscheid, T.M. Koller, M.H. Rausch, A.P. Fröba, Int. J. Hydrogen Energy **47**, 6111 (2022). https://doi.org/10.1016/j.ijhydene.2021.11.198
11. F. Siegert, M. Gundermann, L. Maurer, S. Hahn, J. Hofmann, M. Distel, J. Schühle, K. Müller, M. Wolf, P. Preuster, F. Auer, M. Geißelbrecht, P. Wasserscheid, Int. J. Hydrogen Energy **91**, 834 (2024). https://doi.org/10.1016/j.ijhydene.2024.10.044
12. T. Rüde, S. Dürr, P. Preuster, M. Wolf, P. Wasserscheid, Sustain. Energy Fuels **6**, 1541 (2022). https://doi.org/10.1039/d1se01767e
13. K. Müller, T. Skeledzic, P. Wasserscheid, Energy Fuels **35**, 10929 (2021). https://doi.org/10.1021/acs.energyfuels.1c01170
14. H. Jorschick, M. Geißelbrecht, M. Eßl, P. Preuster, A. Bösmann, P. Wasserscheid, Int. J. Hydrogen Energy **45**, 14897 (2020). https://doi.org/10.1016/j.ijhydene.2020.03.210
15. M. Xu, R. Gao, C. Shi, Z.F. Huang, X. Zhang, J.J. Zou, L. Pan, Chem. Eng. Sci. **287**, 119754 (2024). https://doi.org/10.1016/j.ces.2024.119754
16. S. Pérez-Gil, S. Santos-Moreno, C.D. García, B.M. Madurga, Chem. Eng. Process. **203**, 109904 (2024). https://doi.org/10.1016/j.cep.2024.109904
17. P. Modisha, R. Garidzirai, H. Güneş, S.E. Bozbag, S. Rommel, E. Uzunlar, M. Aindow, C. Erkey, D. Bessarabov, Catalysts **12**, 489 (2022). https://doi.org/10.3390/catal12050489
18. F. Rullo, C.K. Beier, J. Henseler, A. Bösmann, P. Preuster, P. Wasserscheid, M. Geißelbrecht, Int. J. Hydrogen Energy **98**, 606 (2025). https://doi.org/10.1016/j.ijhydene.2024.12.104

19. C.I. Ahn, Y. Kwak, A.R. Kim, M. Jang, A. Badakhsh, J. Cha, Y. Kim, Y.S. Jo, H. Jeong, S.H. Choi, S.W. Nam, C.W. Yoon, H. Sohn, Appl. Catal. B **307**, 121169 (2022). https://doi.org/10.1016/j.apcatb.2022.121169
20. M. Honda, N. Suzuki, Int. J. Environ. Res. Public Health **17**, 1363 (2020). https://doi.org/10.3390/ijerph17041363
21. R. Siewert, A.A. Samarov, S.V. Vostrikov, K. Müller, P. Wasserscheid, S.P. Verevkin, Oxygen **5**, 18 (2025). https://doi.org/10.3390/oxygen5030018
22. A.A. Samarov, K. Müller, P. Wasserscheid, S.P. Verevkin, Chem. Eng. Technol. **47**, 739 (2024). https://doi.org/10.1002/ceat.202300358
23. A. Burgard, M.J. Burk, R. Osterhout, S. Van Dien, H. Yim, Curr. Opin. Biotechnol. **42**, 118 (2016). https://doi.org/10.1016/j.copbio.2016.04.016
24. N. Hirano, R. Tanaka, R. Ukawa-Sato, R.X. Suzuki, J. Freitag, H. Hori, M. Kono, C. Fushimi, ChemistrySelect **10**, e06103 (2025). https://doi.org/10.1002/slct.202406103
25. R. Zhu, G. Zhou, J.N. Teng, W. Liang, X. Li, Y. Fu, Green Chem. **23**, 1758 (2021). https://doi.org/10.1039/d0gc04234j
26. C. Mevawala, T. Autrey, K. Brooks, M. Bowden, B.L. Tran, K. Müller, Energy Fuels **37**, 560 (2023). https://doi.org/10.1021/acs.energyfuels.2c03355
27. V. Gautier, I. Champon, A. Chappaz, I. Pitault, Reactions **3**, 499 (2022). https://doi.org/10.3390/reactions3040033
28. Z. Huang, K.J. Barnett, J.P. Chada, Z.J. Brentzel, Z. Xu, J.A. Dumesic, G.W. Huber, ACS Catal. **7**, 8429 (2017). https://doi.org/10.1021/acscatal.7b03016
29. X. Ren, M. Zhou, W. Yu, M. Zheng, Q. An, Catalysts (2024). https://doi.org/10.3390/catal14050297
30. National Center for Biotechnology Information, PubChem Compound Summary for Gamma-Butyrolactone (CID 7302). https://pubchem.ncbi.nlm.nih.gov/compound/7302. PubChem (2026).
31. S. J. Schwarz W, *Ullmann's Encyclopedia of Industrial Chemistry*, 7th ed. (2005).
32. D.H.S. Ramkumar, A.P. Kudchadker, J. Chem. Eng. Data **34**, 463 (1989). https://doi.org/10.1021/je00058a026
33. J. Wang, C. Ma, X. Ge, Z. Zhong, Q. Zhang, Y. Wei, J. Chem. Eng. Data **70**, 1325 (2025). https://doi.org/10.1021/acs.jced.4c00698
34. F. Chen, Z. Yang, Z. Chen, J. Hu, C. Chen, J. Cai, J. Mol. Liq. **209**, 683 (2015). https://doi.org/10.1016/j.molliq.2015.06.041
35. M. Vraneš, S. Papović, A. Tot, N. Zec, S. Gadžurić, J. Chem. Thermodyn. **76**, 161 (2014). https://doi.org/10.1016/j.jct.2014.03.025
36. G. Moumouzias, C. Ritzoulis, G. Ritzoulis, J. Chem. Eng. Data **44**, 1187 (1999). https://doi.org/10.1021/je990094w
37. S. Boodida, R.K. Bachu, M.K. Patwari, S. Nallani, J. Chem. Thermodyn. **40**, 1422 (2008). https://doi.org/10.1016/j.jct.2008.05.004
38. N. Zec, M. Bešter-Rogač, M. Vraneš, S. Gadžurić, J. Chem. Thermodyn. **97**, 307 (2016). https://doi.org/10.1016/j.jct.2016.02.014
39. B. Hawrylak, S. Andrecyk, C. Gabriel, K. Gracie, R. Palepu, J. Solution Chem. **27**, 827 (1998). https://doi.org/10.1023/A:1022681220744
40. K. Nakanishi, T. Matsumoto, M. Hayatsu, J. Chem. Eng. Data **16**, 44 (1971). https://doi.org/10.1021/je60048a010
41. A. Bagheri, A.A. Rafati, A.A. Tajani, A.R.A. Borujeni, A. Hajian, J. Solution Chem. **42**, 2071 (2013). https://doi.org/10.1007/s10953-013-0093-8
42. K. Liu, B. Li, R. Zhang, Y. Zhang, J. Zhang, J. Iran. Chem. Soc. **19**, 1203 (2022). https://doi.org/10.1007/s13738-021-02371-0
43. L. Kong, B. Li, L. Zhao, R. Zhang, C. Wang, J. Mol. Liq. **326**, 115107 (2021). https://doi.org/10.1016/j.molliq.2020.115107
44. T. Sun, R.M. Digulllo, A.S. Teja, J. Chem. Eng. Data **37**, 246 (1992). https://doi.org/10.1021/je00006a030
45. J. George, N.V. Sastry, J. Chem. Eng. Data **48**, 1529 (2003). https://doi.org/10.1021/je0340755
46. A.K. Nain, Fluid Phase Equilib. **265**, 46 (2008). https://doi.org/10.1016/j.fluid.2007.12.007
47. C. Yang, P. Ma, Q. Zhou, J. Chem. Eng. Data **49**, 582 (2004). https://doi.org/10.1021/je0341918
48. T. Lech, G. Czechowski, J. Jadzyn, J. Chem. Eng. Data **46**, 725 (2001). https://doi.org/10.1021/je0003750

49. D. Mombeini, H.P. Blabus, M.H. Rausch, T. Klein, T.M. Koller, C.J. Kankanamge, M. Geißelbrecht, P. Wasserscheid, A.P. Fröba, Int. J. Thermophys. **47**, 28 (2026). https://doi.org/10.1007/s10765-025-03694-3
50. A. Heller, M.H. Rausch, F. Flohr, A. Leipertz, A.P. Fröba, Int. J. Thermophys. **33**, 396 (2012). https://doi.org/10.1007/s10765-012-1172-6
51. P. Damp, Y. Sun, P.S. Schulz, T.M. Koller, A.P. Fröba, Int. J. Thermophys. **45**, 154 (2024). https://doi.org/10.1007/s10765-024-03453-w
52. P. Damp, Y. Sun, C.J. Kankanamge, J.H. Jander, M.H. Rausch, T. Klein, T.M. Koller, A.P. Fröba, J. Chem. Eng. Data **70**, 4548 (2025). https://doi.org/10.1021/acs.jced.5c00475
53. A.P. Fröba, H. Kremer, A. Leipertz, J. Phys. Chem. B **112**, 12420 (2008). https://doi.org/10.1021/jp804319a
54. B. Hasse, J. Lehmann, D. Assenbaum, P. Wasserscheid, A. Leipertz, A.P. Fröba, J. Chem. Eng. Data **54**, 2576 (2009). https://doi.org/10.1021/je900134z
55. M. Kerscher, J.H. Jander, J. Cui, L.A. Maurer, P. Wolf, J.D. Hofmann, A. Köksal, H. Zachskorn, F. Auer, P.S. Schulz, P. Wasserscheid, M.H. Rausch, T.M. Koller, A.P. Fröba, Int. J. Hydrogen Energy **77**, 1009 (2024). https://doi.org/10.1016/j.ijhydene.2024.06.131
56. T.M. Koller, J.H. Jander, C.J. Kankanamge, L.M. Braun, P.K. Chittem, M. Kerscher, M.H. Rausch, T. Klein, P. Wasserscheid, A.P. Fröba, Int. J. Thermophys. **45**, 156 (2024). https://doi.org/10.1007/s10765-024-03449-6
57. A.P. Fröba, S. Will, Y. Nagasaka, J. Winkelmann, S. Wiegand, in *Experimental Thermodynamics*, edited by J.M. Assael, A.R.H. Goodwin, V. Vesovic, W.A. Wakeham (Royal Society of Chemistry, 2014), pp. 19–74.
58. J. Cui, M. Kerscher, J.H. Jander, T. Rüde, P.S. Schulz, P. Wasserscheid, M.H. Rausch, T.M. Koller, A.P. Fröba, J. Chem. Eng. Data **67**, 3085 (2022). https://doi.org/10.1021/acs.jced.2c00519
59. J. Cui, J.H. Jander, T.M. Koller, A.P. Fröba, J. Chem. Eng. Data **67**, 644 (2022). https://doi.org/10.1021/acs.jced.1c00946
60. T.M. Koller, M. Kerscher, A.P. Fröba, J. Colloid Interface Sci. **626**, 899 (2022). https://doi.org/10.1016/j.jcis.2022.06.129
61. A.P. Fröba, A. Leipertz, Diffus. Fundam. **2**, 63 (2005). https://doi.org/10.62721/diffusion-fundamentals.2.249
62. M. Kerscher, A.P. Fröba, T.M. Koller, Int. J. Thermophys. **42**, 159 (2021). https://doi.org/10.1007/s10765-021-02909-7
63. D.A. Long, *The Raman Effect: A Unified Treatment of the Theory of Raman Scattering by Molecules* (Wiley, Chichester, 2002). https://doi.org/10.1002/0470845767.fmatter_indsub
64. M.J. Pelletier, Appl. Spectrosc. **57**, 20A (2003). https://doi.org/10.1366/000370203321165133
65. J.H. Jander, M. Kerscher, S. Li, M.H. Rausch, P. Wasserscheid, A.P. Fröba, Int. J. Hydrogen Energy **47**, 9331 (2022). https://doi.org/10.1016/j.ijhydene.2022.01.005
66. J.H. Jander, P.K. Chittem, M. Kerscher, M.H. Rausch, P. Wasserscheid, A.P. Fröba, Int. J. Hydrogen Energy **73**, 681 (2024). https://doi.org/10.1016/j.ijhydene.2024.05.381
67. H. Hase, K. Ishioka, Y. Miyatake, M. Kobayashi, M. Kobayashi, J. Phys. Chem. **95**, 8541 (1991). https://doi.org/10.1021/j100175a025
68. D.K. Singh, S. Mishra, A.K. Ojha, S.K. Srivastava, S. Schlücker, B.P. Asthana, J. Popp, R.K. Singh, J. Raman Spectrosc. **42**, 667 (2011). https://doi.org/10.1002/jrs.2744
69. V. Dracopoulos, G.N. Papatheodorou, Phys. Chem. Chem. Phys. **2**, 2021 (2000). https://doi.org/10.1039/b000803f
70. S. Beck, M. Feller, L. Spies, K.J. Dietrich, C. Jessen, K. Stierstorfer, A.J. Kornath, ChemistryOpen **10**, 8 (2021). https://doi.org/10.1002/open.202000220
71. R.R. Shagidullin, A.V. Chernova, R.R. Shagidullin, A.E. Arbuzov, Russ. Chem. Bull. **42**, 1505 (1993). https://doi.org/10.1007/BF00699184
72. S.M.I. Saad, A.W. Neumann, Adv. Colloid Interface Sci. **238**, 62 (2016). https://doi.org/10.1016/j.cis.2016.11.001
73. J.H. Jander, P.S. Schmidt, C. Giraudet, P. Wasserscheid, M.H. Rausch, A.P. Fröba, Int. J. Hydrogen Energy **46**, 19446 (2021). https://doi.org/10.1016/j.ijhydene.2021.03.093
74. M. Kerscher, J.H. Jander, J. Cui, M.M. Martin, M. Wolf, P. Preuster, M.H. Rausch, P. Wasserscheid, T.M. Koller, A.P. Fröba, Int. J. Hydrogen Energy **47**, 15789 (2022). https://doi.org/10.1016/j.ijhydene.2022.03.051
75. M. Kerscher, L.M. Braun, J.H. Jander, M.H. Rausch, T.M. Koller, P. Wasserscheid, A.P. Fröba, Int. J. Thermophys. **45**, 8 (2024). https://doi.org/10.1007/s10765-023-03294-z

76. C. Qasmi, R. Mochel, V. Gautier, I. Champon, S. Thomas, A. Chappaz, R. Anne-Cécile, Int. J. Hydrogen Energy **67**, 829 (2024). https://doi.org/10.1016/j.ijhydene.2023.11.232
77. N. Ichikawa, S. Sato, R. Takahashi, T. Sodesawa, K. Inui, J. Mol. Catal. A Chem. **212**, 197 (2004). https://doi.org/10.1016/j.molcata.2003.10.028
78. J.H. Schlander, T. Turek, Ind. Eng. Chem. Res. **38**, 1264 (1999). https://doi.org/10.1021/ie980606k
79. T.M. Koller, M. Kerscher, A. Köksal, M.R. Stockerl, T. Klein, A.P. Fröba, J. Phys. Chem. B **127**, 10647 (2023). https://doi.org/10.1021/acs.jpcb.3c06309
80. A. Sharma, N. Deepika, S. Pandey, J. Chem. Eng. Data **69**, 3747 (2024). https://doi.org/10.1021/acs.jced.4c00259
81. International Association for the Properties of Water and Steam, *Revised Release on Surface Tension of Ordinary Water Substance* (Moscow, Russia, 2014), IAPWS R1-76. https://iapws.org/documents/release/Surf-H2O.
82. J. Vijande, M.M. Piñeiro, J. García, J.L. Valencia, J.L. Legido, J. Chem. Eng. Data **51**, 1778 (2006). https://doi.org/10.1021/je060179e
83. T.M. Koller, M.H. Rausch, A.P. Fröba, Int. J. Thermophys. **45**, 57 (2024). https://doi.org/10.1007/s10765-024-03344-0
84. Z. Mužíková, P. Šimáček, M. Pospíšil, G. Šebor, J. Fuels **2014**, 459287 (2014). https://doi.org/10.1155/2014/459287
85. C.Y. Tsai, A.N. Soriano, M.H. Li, J. Chem. Thermodyn. **41**, 623 (2009). https://doi.org/10.1016/j.jct.2008.12.022
86. C. Zhu, Z. Zhang, S. Xue, K. Hou, H. Liu, X. Liu, M. He, Fuel **316**, 123425 (2022). https://doi.org/10.1016/j.fuel.2022.123425
87. M. Lifi, I. Abala, R. Briones-Llorente, N. Munoz-Rujas, F. Aguilar, F.E.M. Alaoui, J. Chem. Eng. Data **68**, 3062 (2023). https://doi.org/10.1021/acs.jced.3c00320
88. L.C. Wilson, H.L. Wilson, W.V. Wilding, G.M. Wilson, J. Chem. Eng. Data **41**, 1252 (1996). https://doi.org/10.1021/je960052x
89. C. Tegeler, R. Span, W. Wagner, J. Phys. Chem. Ref. Data **28**, 779 (1999). https://doi.org/10.1063/1.556037

Publisher's Note Springer Nature remains neutral with regard to jurisdictional claims in published maps and institutional affiliations.

Authors and Affiliations

Yongzhen Sun[1] · Julius Hans Jander[1] · Yang Xie[1] · Muhammad Junaid Akhtar[1] · Michael Heinrich Rausch[1] · Michael Geißelbrecht[2] · Peter Wasserscheid[2,3,4] · Andreas Paul Fröba[1]

✉ Andreas Paul Fröba
andreas.p.froeba@fau.de

[1] Department of Chemical and Biological Engineering (CBI) and Erlangen Graduate School in Advanced Optical Technologies (SAOT), Institute of Advanced Optical Technologies – Thermophysical Properties (AOT-TP), Friedrich-Alexander-Universität Erlangen-Nürnberg (FAU), Paul-Gordan-Straße 8, 91052 Erlangen, Germany

[2] Forschungszentrum Jülich GmbH, Helmholtz Institute Erlangen-Nürnberg for Renewable Energy (IET-2), Cauerstraße 1, 91058 Erlangen, Germany

[3] Department of Chemical and Biological Engineering (CBI), Institute of Chemical Reaction Engineering (CRT), Friedrich-Alexander-Universität Erlangen-Nürnberg (FAU), Egerlandstraße 3, 91058 Erlangen, Germany

[4] Forschungszentrum Jülich GmbH, Institute for a Sustainable Hydrogen Economy, Am Brainergy Park 4, 52428 Jülich, Germany